Journal of Volcanology and Geothermal Research xxx (2009) xxx–xxx

Contents lists available at ScienceDirect

Journal of Volcanology and Geothermal Research

journal homepage: www.elsevier.com/locate/jvolgeores

Retrieval of volcanic ash particle size, mass and optical depth from a ground-based thermal infrared camera

A.J. Prata [a,*], C. Bernardo [b]

[a] Norwegian Institute for Air Research, PO Box 100, 2027 Kjeller, Norway
[b] Auspace Ltd, PO Box 17, Mitchell, ACT 2911, Australia

ARTICLE INFO

Article history:
Received 2 June 2008
Accepted 19 February 2009
Available online xxxx

ABSTRACT

Volcanoes can emit fine-sized ash particles (1–10 μm radii) into the atmosphere and if they reach the upper troposphere or lower stratosphere, these particles can have deleterious effects on the atmosphere and climate. If they remain within the lowest few kilometers of the atmosphere, the particles can lead to health effects in humans and animals and also affect vegetation. It is therefore of some interest to be able to measure the particle size distribution, mass and other optical properties of fine ash once suspended in the atmosphere. A new imaging camera working in the infrared region between 7–14 μm has been developed to detect and quantify volcanic ash. The camera uses passive infrared radiation measured in up to five spectral channels to discriminate ash from other atmospheric absorbers (e.g. water molecules) and a microphysical ash model is used to invert the measurements into three retrievable quantities: the particle size distribution, the infrared optical depth and the total mass of fine particles. In this study we describe the salient characteristics of the thermal infrared imaging camera and present the first retrievals from field studies at an erupting volcano. An automated ash alarm algorithm has been devised and tested and a quantitative ash retrieval scheme developed to infer particle sizes, infrared optical depths and mass in a developing ash column. The results suggest that the camera is a useful quantitative tool for monitoring volcanic particulates in the size range 1–10 μm and because it can operate during the night, it may be a very useful complement to other instruments (e.g. ultra-violet spectrometers) that only operate during daylight.

1. Introduction

Volcanic ash is a known hazard to human and animal health (Baxter, 1999), can affect the climate and atmosphere (Robock, 2000) and is a threat to aviation safety (Casadevall, 1994). Ash particles suspended in the atmosphere occupy a range of sizes from small (μm size) to large (mm to cm size). The largest particles fall out of the atmosphere relatively quickly-particles with radii >50 μm fall out under gravitational settling within a few hours (Schneider et al., 1999), whereas the smallest particles (r<0.1 μm) may remain in the atmosphere for many days or weeks. Other processes may increase or decrease the removal of fine particles from the atmosphere. For example, coagulation can speed up removal, while vertical wind and rapid horizontal transport can prolong the atmospheric lifetime of fine particles.

The climate effects of ash particles have not been studied in any detail, but it is known that ash can suppress surface temperatures by several degrees during the day and enhance them by night (Robock and Mass, 1982). It used to be thought that fine ash particles were responsible for the observed global cooling following very large volcanic eruptions (Lamb, 1970). It is now believed that sulphate particles suspended in the stratosphere are the main cause of the cooling (Robock, 2000). However, very small ash particles (r<0.1 μm) can have long residence times and also absorb and scatter radiation, and local climate and weather may be affected by ash in the atmosphere (Robock and Mass, 1982), by blocking out solar radiation and absorbing and re-emitting infrared radiation. The precise interplay between the solar and thermal radiation fields depends on the ash microphysics as well as the quantity, vertical distribution and residence time of the ash.

Volcanic ash is mostly composed of silicon dioxide (SiO_2) accompanied by other minerals in small amounts. Some of the SiO_2 remains unattached to other elements and this "free" crystalline silica can cause silicosis. Typically the "free" silica represents less than 10% of the ash by weight, while the ash itself may contain up to ~80% SiO_2. The US National Institute for Occupational Safety and Health have recommended an exposure limit of 50 μg m^{-3} of "free" silica for a 40-hour work week over a lifetime. Given the lower free silica content of respirable ash, this is equivalent to an exceedance limit of 1 mg m^{-3}. We will see later that this limit can be easily reached during ash-fall.

In locales where there is on-going volcanic activity leading to continuous or semi-continuous ash emissions further hazards are created. These include disruption of routine business and social life,

* Corresponding author.
E-mail address: fred.prata@nilu.no (A.J. Prata).

0377-0273/$ – see front matter © 2009 Elsevier B.V. All rights reserved.
doi:10.1016/j.jvolgeores.2009.02.007

degradation of infrastructure (e.g. road and building damage), contamination of potable water, damage to power supplies, loss of trade and transport through disruption at airports, and an increase in respiratory problems due to longterm exposure to airborne ash. For many of these hazards it is important to know the range of particle sizes, the mass loading and the total mass of ash. For aviation it is also useful to know the vertical distribution, horizontal transport and effect on visibility.

Throughout the remainder of this paper we will restrict the discussion of volcanic ash to particles with radii (r) in the size range $1 < r < 10$ μm and a composition of ~60% bound SiO_2. This is because our discussion will focus on the use of thermal infrared radiation with wavelengths (λ) in the range 7–14 μm and this range is optimal for detecting SiO_2 particles with radii, $r \approx \lambda$. This particle range is also the size range most likely to cause turbine engine failure in commercial jet aircraft (Casadevall et al., 1996) and also within the range of respirable particle sizes.

The paper is organised as follows: a description of a new thermal infrared imaging camera is provided, giving the important details of its operation and use as a volcanic ash detector. Some details of the data analysis, instrument calibration and processing are given next. The two main operating modes of the camera are described with details of the ash discrimination algorithm followed by a mathematical treatment of the ash microphysical retrieval scheme. Results from using the camera at the site of an erupting volcano are presented and we conclude with some ideas about how the system may be deployed at volcano observatories, airports at risk from volcanic activity and as a complementary device to other volcano monitoring tools.

2. Thermal infrared imaging camera

A camera system utilising passive infrared radiation was developed following original concepts based on the work of Prata (1989b) and Prata and Barton (1993) which showed how spectrally filtered infrared radiation could be used to discriminate volcanic ash from meteorological clouds. That work was focussed on using satellite and airborne measurements and we extend that here to an instrument that can be used from the ground.

Thermal imaging cameras based on uncooled microbolometer array technology are commercially available with temperature sensitivities of 50 mK (8–12 μm), array sizes of 320×240 pixels, F1.0 optics and 60 Hz operation (Kruse, 2001). In principle a camera of this kind can acquire images showing temperature changes of less than 0.1 K at a rate of 10's of frames per second. Frame rates as high as this are not necessarily needed, but it may be desirable to achieve multiple images per minute because of the fast dynamics of erupting volcanic ash columns. In practice it is difficult to achieve very high frame rates (30–60 Hz) from these cameras because of the presence of noise ($1/f$, background and internal temperature fluctuations, and Johnson noise), which can be alleviated by frame integration. Other factors may also limit achieving high image capture rates: for example extracting the image frame data rapidly requires fast electronics and a good microprocessor and communications hardware and software. The camera that we have used also incorporates wavelength selection (filters) and this adds time delays to the image capture. The prototype design is restricted to image capture rates of 1 every 5–6 min, which is too slow for studying the dynamics of ash column development but adequate (as we will show) for determining the ash microphysics. The slow data rate of the prototype instrument is simply a product of the data transfer system and can easily be overcome with better communication electronics.

2.1. Cyclops — a multifilter thermal infrared camera system

Thermal IR cameras with 50 mK noise-equivalent temperature difference (NEΔT) are available commercially. Commercial off-the-shelf (COTS) cameras come with a single, broadband filter covering the IR wavelength region from 7 μm to about 14 μm, which is regarded as a region of relatively high atmospheric transparency. The camera was designed to measure both atmospheric gases (SO_2 in particular) and volcanic ash. Details of the algorithms and test results for using Cyclops to measure volcanic SO_2 are provided in a separate paper (Prata and Bernardo, submitted for publication). For use in detecting and quantifying particles at typical atmospheric temperatures (230–300 K), several modifications to the COTS camera were needed. The two most important of these modifications are described below.

Fig. 1. Cyclops filter wheel and interference filters. The current arrangement has 5 filters with central wavelengths at 7.34, 8.55, 10, 11, 12 μm. For operations from the ground, the 7.34 μm filter was replaced with a broadband filter covering 7–14 μm.

2.2. Filtering

Spectral selection of radiation into narrow bands (0.5–1.0 μm) is achieved by placing a filter wheel between the fore-optics and detector. A photograph showing the filters and filter wheel engineered to fit to the COTS camera is provided in Fig. 1. The filters are carefully selected to match pre-determined specifications for optimal sensing of SO_2 gas and volcanic ash particles, the two major hazardous components of volcanic emissions. For detecting the presence of ash particles we draw on previous studies (e.g. Prata, 1989a,b; Wen and Rose, 1994; Prata and Grant, 2001) that have exploited the fact that silicate particles undergo a differential absorption effect as a function of wavelength that is opposite to water vapour. Fig. 2 shows the absorption spectrum of some mixed phase clouds compared with a spectrum of ash determined from the Atmospheric Infrared Sounder (AIRS) satellite sensor (Chahine et al., 2006). Only the "window" region between 800–1100 cm^{-1} is shown as this region is most strongly affected by silicate ash and meteorological clouds.[1] Notice that the ash absorption spectrum increases with increasing wavenumber, while the spectrum of mixed phase cloud shows no change or perhaps a slight decrease with wavenumber. Indeed for ice clouds, the slope of the absorption spectrum is sensitive to particle size and exhibits a marked decrease with increasing wavenumber (Huang et al., 2004). These differing effects permit easy identification of ash

[1] Wavenumber (ν) is used in preference to wavelength (λ) here for consistency with the AIRS literature. The conversion is: $\lambda\ (\mu m) = 10{,}000/\nu\ (cm^{-1})$.

Please cite this article as: Prata, A.J., Bernardo, C., Retrieval of volcanic ash particle size, mass and optical depth from a ground-based thermal infrared camera, J. Volcanol. Geotherm. Res (2009), doi:10.1016/j.jvolgeores.2009.02.007

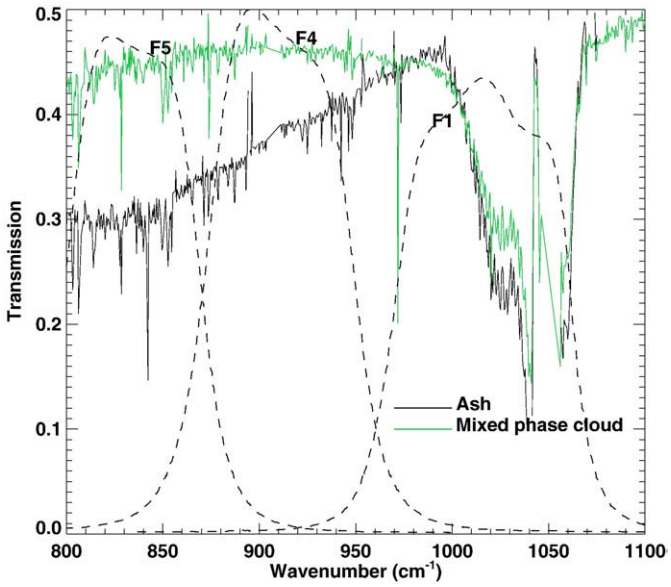

Fig. 2. Atmospheric transmission spectra for an ash cloud and a mixed phase cloud, measured from the AIRS (Atmospheric Infra-Red Sounder) satellite sensor. Notice the characteristic decrease in absorption with wavenumber from about 800 cm^{-1} to about 1000 cm^{-1} for volcanic ash and the almost flat slope of the mixed phase cloud. Also shown are the filter response functions (arbitrary units) for three of the Cyclops channels.

from water vapour, water droplets and ice particles and, as we will show, the potential to determine particle radii sizes, optical depths and mass loadings. Also shown on Fig. 2 are the filter response functions for three of the Cyclops filters, centred at 10, 11 and 12 μm (see also Table 1).

The design of Cyclops was heavily influenced by knowledge of atmospheric gas and particle absorption and constrained by current technology. The most important consideration in the design of Cyclops was the choice of the number of filters required, the filter central wavelengths and the filter widths. Interference filters operating in the wavelength band 7–14 μm are readily available. A series of calculations was performed to find wavelengths and filter widths to optimise the signal due to ash. The main constraint on the widths of the filters are the signal-to-noise (SNR) ratio (broader filters provide greater energy and hence better SNR), but the filters must not be too broad that adjacent filters overlap introducing unwanted correlations between channels. Radiative transfer simulations suggest that to achieve NEΔT's of <100 mK at 290 K, the filters need to be ≈1.0 μm wide assuming additional time integration (30–60 frame averaging) could be employed. The central wavelengths were determined through radiative transfer simulations (see Prata and Barton, 1993). For the SO_2 channel the choice was governed by ensuring that the entire 8.6 μm SO_2 absorption feature was included. This meant a narrower filter was needed (≈1 μm) which had the additional advantage that more energy is collected; since there is less energy at 8.6 μ than at 11 or 12 μm. Even so, the resulting NEΔT is on the high side of what would be optimal. Making the filter any broader allows too much interference from water vapour and the trade-off between higher NEΔT and reducing water vapour effects was a limiting factor in the choice of the SO_2 filter. The number of filters required (3 for ash and 1 for SO_2) was also determined through radiative transfer calculations. A broadband filter was deemed useful based on the lower NEΔT and the usefulness of this channel for general thermal imaging. Table 1 shows the channels (or narrow bands) chosen for Cyclops for detecting ash and SO_2 from the ground. As we do not have high spectral resolution infrared measurements of ash clouds from ground-based sensing, the selection of filters was influenced by satellite measurements (as illustrated in Fig. 2) and by the radiative transfer and technical trade-offs mentioned earlier. The 10 μm filter (F1 on Fig. 2), includes a strong absorption feature due to O_3, which we would not expect to see from a ground-based sensor. Filters F4 and F5 capture the absorption change between ash and meteorological clouds, and as with ice, the slope of the ash absorption curve is also sensitive to particle size. Finally, since the measurements from a ground-based instrument view the ash cloud with cold background, the variation of absorption with wavenumber for ash will be opposite to that shown from the space-borne measurements (Fig. 2).

Table 1
Channel number, central wavelength, bandwidth, purpose and required noise equivalent temperature difference (NEΔT) for Cyclops.

Channel number	Wavelength (μm)	Bandwidth (μm)	Purpose	Required NEΔT (mK)
1	10.0	1	Cloud-base temperature	100
2	7–14	7	Cloud imaging	50
3	8.6	0.5	SO_2	300
4	11.0	1	Volcanic ash	100
5	12.0	1	Volcanic ash	100

3. Calibration, data analysis and processing

3.1. Calibration

Gas and particle discrimination and quantification requires high fidelity thermal images from Cyclops. To achieve reliability and accuracy the camera must be calibrated. The calibration procedure that we have adopted is both novel and somewhat complex. It is the subject of a separate paper (Bernardo and Prata, 2008) and here we just provide the basic details.

The procedure is a linear calibration requiring an estimate of the gain and intercept that converts the digital numbers (DNs) to radiances and then to brightness temperatures. A two-step process is implemented: Cyclops is first calibrated in the laboratory under controlled conditions using a blackbody source and estimates of the gains and intercepts for all channels are determined for a variety of environmental and target (source) conditions. In the field, environmental conditions cannot be measured well enough to allow use of these calibration coefficients alone. Thus a second step is employed that compensates for changes in the environmental conditions, specifically, the temperatures of the instrument, fore-optics and outer housing. This second step requires the addition of a blackbody shutter, placed in front of the fore-optics, filter wheel and detector. The temperature controlled shutter moves in front of the camera on computer command, to allow a single calibration point on the DN-radiance calibration line. The calibration can be repeated as frequently as required and is performed for each of the five filters separately. This two-step procedure gives temperature precisions of 0.2 to 0.7 K at 280 K, depending on channel.

3.2. Data analysis and processing

The 2D image data (320×240 pixels) acquired from the camera consist of raw digital numbers (DNs) for each channel (or filter) and after calibration are converted to scene brightness temperatures (BTs) using a look-up table procedure that relates the DNs to the radiance integrated over the filter response function. The range of validity and accuracy of this procedure varies with channel, but for temperatures between 260–290 K accuracies are better than 0.1 K.

After calibration and conversion to BTs, each measurement sequence consists of 5 BT images acquired at 5–6 min intervals over time periods of up to many hours. Fig. 3 illustrates the quick-look analysis for one measurement set, which shows a mostly clear-sky scene, with a few low clouds. The panels on the left-hand side show

Please cite this article as: Prata, A.J., Bernardo, C., Retrieval of volcanic ash particle size, mass and optical depth from a ground-based thermal infrared camera, J. Volcanol. Geotherm. Res (2009), doi:10.1016/j.jvolgeores.2009.02.007

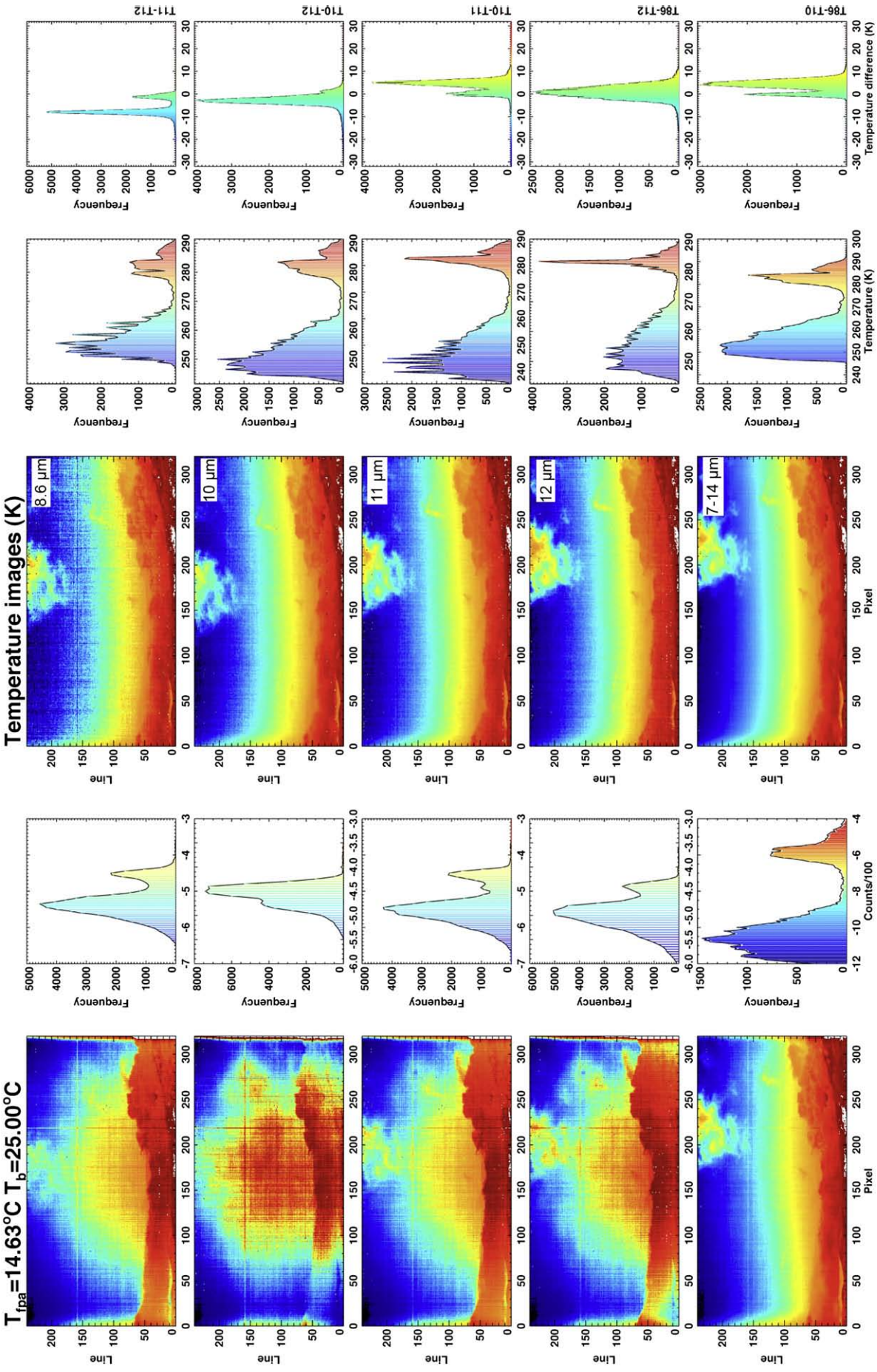

Fig. 3. Cyclops quick-look images. First column: raw image with digital numbers scaled from lowest in blue to highest in red. Second column: image histograms for the raw data, Third column: calibrated brightness temperature images (in Kelvin) with coldest values in blue and warmest values in red. Fourth column: brightness temperature histograms for the calibrated data. All five channels are shown, starting from top: 8.55, 10, 11, 12 and 7–14 μm. Fifth column: brightness temperature difference histograms for the calibrated data. The combinations shown, starting from top are: $T_{11}-T_{12}$, $T_{10}-T_{12}$, $T_{10}-T_{11}$, $T_{8.6}-T_{12}$ and $T_{8.6}-T_{10}$.

Please cite this article as: Prata, A.J., Bernardo, C., Retrieval of volcanic ash particle size, mass and optical depth from a ground-based thermal infrared camera, J. Volcanol. Geotherm. Res (2009), doi:10.1016/j.jvolgeores.2009.02.007

raw DN images and their respective histograms and those on the right hand-side show BT images after calibration and conversion, with a set of temperature difference histograms. All channels are shown, from the top down these are: 8.6, 10, 11, 12 μm and broadband (7–14 μm). It can be seen that the calibrated (temperature) images now contain information with many of the camera artifacts (optical distortions, pixel inhomogeneities etc.) minimised. The images also indicate the general trend of decreasing radiation (at all wavelengths) with increasing viewing elevation angle. The rate of decrease with elevation angle is not the same at all wavelengths and the atmosphere induces a differential absorption effect that depends on viewing angle. The importance of calibrating the images is also apparent. The semi-circular patches appearing in the centre of the filtered raw images is caused by unwanted radiation from the lens and housing of Cyclops. There is also an artifact at the left-edge of the uncalibrated data, which has been largely removed in the calibrated data. The image histograms show the range of temperatures measured in this scene is quite broad, from ~250 to ~300 K. The difference histograms are used to identify features in the imagery, in particular the 11–12 μm differences are used to identify ash from clear and cloudy skies (see later for details). Finally, it can be seen that image noise is higher at 8.6 μm and lowest in the broadband (lowest panel) image.

These general observations lead to two very significant conclusions regarding the subsequent processing of the Cyclops data. Firstly, raw, uncalibrated data is virtually of no value for identifying gases or particulates in these filtered thermal IR images. Since much of the useful information is contained in difference images, reducing noise and applying a consistent and accurate calibration appear to be fundamental to transforming the data into information. Secondly, we note the strong affect water vapour has on the measurements. Water vapour alters the amount of radiation reaching the target. It can both absorb and emit radiation and the contribution from water vapour to the signal at the detector will depend on the water vapour pathlength and its temperature. Applying an atmospheric correction is crucial to correctly identifying ash in the images. Furthermore the correction must be applied with a dependence on viewing angle and preferably on a pixel-by-pixel basis.

4. Ash detection algorithm

The general theory for discriminating and quantifying ash in volcanic plumes using satellite measurements has been described in detail by Prata (1989a,b) and Prata and Grant (2001). The complementary theory for ground-based and airborne devices has been described previously by Prata and Barton (1993). The basic idea behind discriminating ash in volcanic plumes, from all other constituents, most notably water vapour and water droplets rests on the observation that for water vapour, IR absorption increases with wavelength, while for silicates the reverse is true. Thus by comparing radiation at two, well-chosen wavelengths, a simple binary decision based algorithm can be used, i.e.:

$$\Delta T = T_i - T_j, \tag{1}$$

where T_i and T_j are two brightness temperatures measured in Cyclops channels λ_i and λ_j, with,

$\lambda_i < \lambda_j$.

Then,

$\Delta T < \Delta T_{cut} \rightarrow$ water vapor

$\Delta T > \Delta_{cut} \rightarrow$ volcanic ash.

In practice the cut-off temperature difference (ΔT_{cut}) will depend on atmospheric conditions and it is known that viewing geometry also has a significant effect. There are two modes of operation for Cyclops when viewing ash-rich plumes: (1) discrimination mode, and (2) microphysics mode. Mode (1) allows Cyclops to quickly infer the presence of ash and if rapid sampling is available, information on ash movement and direction of travel can be inferred and communicated to a user; for example at an airport or a distant volcanological observatory. Mode (2) provides information to researchers interested in volcanological processes and could be helpful to emergency services in populated regions where high atmospheric ash loadings may cause respiratory or other deleterious health effects. Cyclops has been tested in Mode (1) operation, using an automatic statistical histogram test, while a more sophisticated physical methodology has been developed for generating Mode (2) products from Cyclops.

Water vapour is typically the largest absorber and emitter of radiation within the Cyclops wavebands. Corrections to the Cyclops measurements for the effects of water vapour are made using a radiative transfer model that takes into account the viewing geometry and background environmental conditions. To make these corrections, ancillary data in the form of radiosonde measurements must be available. However, such data are not always available or even appropriate for some of the viewing conditions encountered during the field trials. When radiosonde data are available, the corrections are made to account for absorption and emission along the path between the camera and target (the volcanic ash) and the calibrated brightness temperature images are replaced by atmospherically corrected brightness temperature images. More detail on the correction procedure can be found in Prata and Bernardo (submitted for publication).

Viewing from the ground exacerbates the problem of water vapour because the concentration is largest near the surface and decreases rapidly (exponentially) with increasing height above the surface. At low elevation viewing angles (high zenith angles) the water vapour path length, the product of the water vapour amount and geometrical pathlength, can be large and hence have a significant effect on the measured IR radiation. Furthermore, water vapour absorbs differentially across the waveband, with greater absorption (and emission) occurring at 12 μm than at 11 μm. Since Cyclops views the water vapour against a sky background that is usually colder than the foreground, in the absence of other absorbers (e.g. ash), Cyclops measures more radiation at 12 μm than at 11 μm. This feature is utilised to provide a fast mechanism for deciding on whether ash is present in a Cyclops image. The procedure is automated and operates on all pixels within the image. The methodology uses a simple statistical test in which a Gaussian distribution (or set of distributions) is used to fit the temperature difference image histogram and an "alarm" is triggered based on some predefined threshold values (see Section 5).

5. Ground-based IR sensing

The Cyclops camera operates from a fixed position on the ground and views the target from some distance (up to 10 km). The actual location of the camera relative to the target is, of course, completely selectable. However, certain considerations are needed if the system is to operate in a useful manner. For example, it may be sensible to place the camera so that it has a fixed view of the volcano under study and so that ash columns and clouds can be simultaneously observed. Alternatively it may be preferable at airports to site the camera so that it views vertically upwards or at a high elevation angle towards a nearby volcano. Each of the multitude of different viewing orientations may induce adverse effects into the analysis of the data. These might include fixed obstructions within the field of view (trees, buildings, terrain etc.) and or ephemeral problems due to the effects of meteorological clouds or water vapour. The many possible viewing orientations make it difficult to provide a single

Please cite this article as: Prata, A.J., Bernardo, C., Retrieval of volcanic ash particle size, mass and optical depth from a ground-based thermal infrared camera, J. Volcanol. Geotherm. Res (2009), doi:10.1016/j.jvolgeores.2009.02.007

formula or algorithm to account for all potential adverse viewing effects.

The effect of fixed obstructions (trees, buildings, terrain etc.) can be accounted for by taking a reference image on a clear day. A mask can be generated from this image and then used to highlight or delineate the portions of the image showing the obstructions. This process was done for the images acquired at Tavurvur volcano, New Britain presented later (see Figs. 17–21).

The water vapour path length effects can be accounted for if the distance to the target (e.g. ash plume or cloud) and orientation of the camera are known. An estimate of the water vapour structure of the local atmosphere must also be known and can usually be obtained form a nearby radiosounding. The orientation of the camera can be found from simple geometrical considerations. Fig. 4 shows a schematic of the geometry of imaging a slab of plume from a fixed ground-based position. The coordinate system adopted is Cartesian with the leading side of the plume placed at $y=0$, the camera placed at $x=0$, $y=L$, $z=0$ and the coordinates x and y represent the horizontal axes and z the vertical axis as shown in Fig. 4. The camera views the plume from a distance R, measured from the centre of the detector to the side of the plume closest to the camera, and at an elevation angle θ_n and azimuth angle ϕ_n, which vary with camera pixel number n. In this coordinate system the camera line C_l and column C_c numbers are related to the camera elevation and azimuth angles through:

$$C_l = \frac{L}{s_n}(\cos\phi_n \tan\theta_n - \tan\zeta) \tag{2}$$

$$C_c = \frac{N_c}{2} + \frac{L}{s_n}\tan\phi_n \tag{3}$$

$$n = C_c + N_c(C_l - 1), \tag{4}$$

where L is the distance to the plume measured in the x–y plane ($z=0$), ζ is the elevation of the camera measured from ground level (height above mean sea level) to the first line of the image, s_n is the size of image pixel n, and the image has N_c columns by N_l lines (320×240 in the current setup). The camera is oriented such that an azimuth angle of $\phi_n=0$ corresponds to the centre of the image, or column number $N_c/2$. Pixel numbers are counted from the bottom left of the image with line 1, column 1 corresponding to pixel number 1 and the last column of the top line corresponding to pixel number N_c

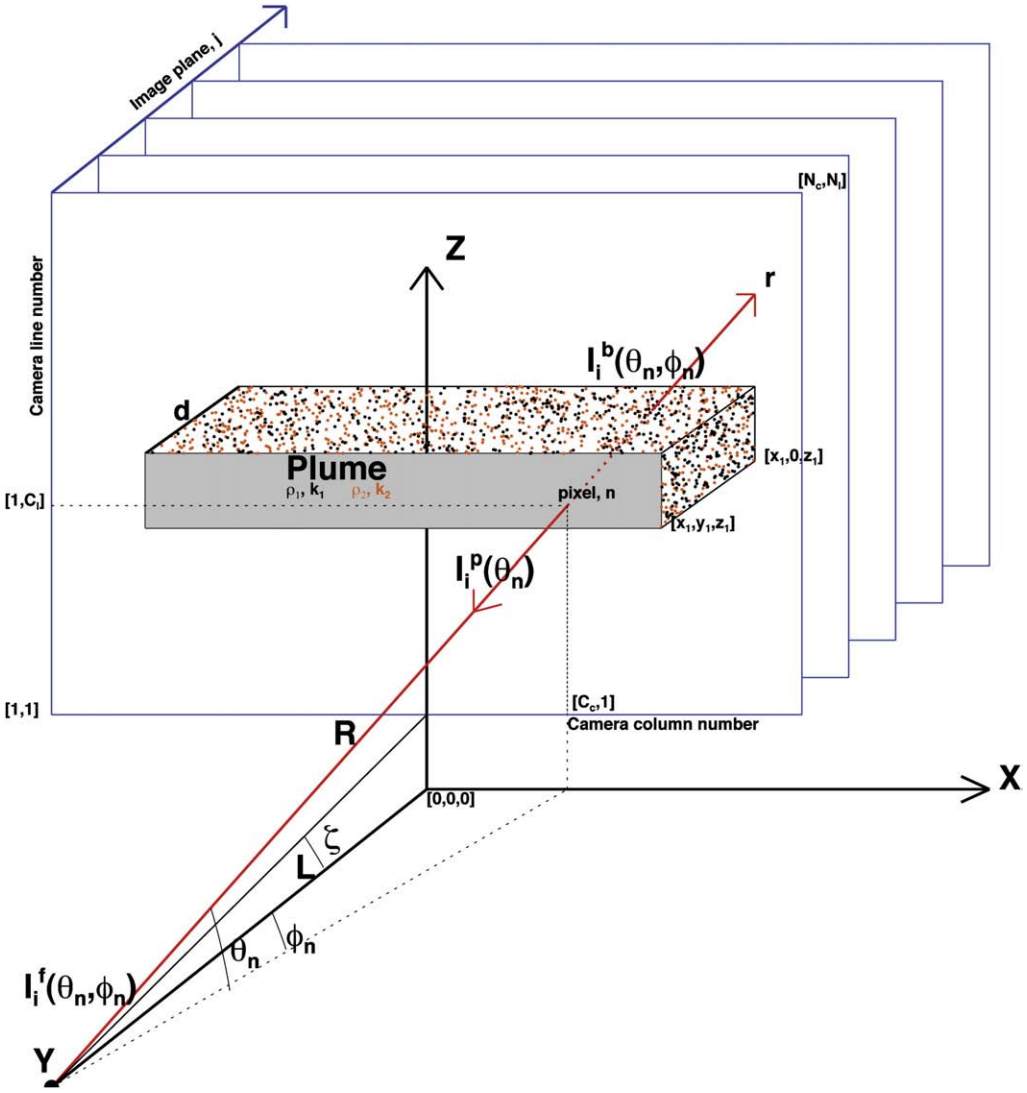

Fig. 4. Measurement geometry for a thermal camera viewing an 'idealized' plane-parallel volcanic cloud. The camera is at position Y and all symbols are defined in the text.

Please cite this article as: Prata, A.J., Bernardo, C., Retrieval of volcanic ash particle size, mass and optical depth from a ground-based thermal infrared camera, J. Volcanol. Geotherm. Res (2009), doi:10.1016/j.jvolgeores.2009.02.007

N_l. The pixel size varies with line and column number and can be determined from:

$$s_{l,c} = \frac{L}{N_{l,c}} \tan\left(\frac{\Psi_{l,c}}{2}\right), \quad (5)$$

$$\Psi_{l,c} = 2\tan^{-1}\left(\frac{N_{l,c}\chi}{2F}\right), \quad (6)$$

where F is the focal length of the camera, χ is the pitch of the pixel on the detector chip (~45 μm), and $\Psi_{l,c}$ is the field-of-view of the microbolometer detector array in the vertical (Ψ_l) or horizontal (Ψ_c). In this idealised model of the plume, the radiation measured at the imager can be described by three terms:

$$I_i(\theta) = I_i^f(\theta,\phi) + I_i^p(\theta,\phi) + I_i^b(\theta,\phi), \quad (7)$$

where θ is elevation angle, ϕ is azimuth angle, i is channel number, and the superscripts refer to foreground radiance (f), background (b), and plume radiance (p). The plume radiance may be considered to consist of emitted radiation, and radiation from the atmosphere that has been attenuated as it traverses through the plume. Scattering is ignored. The channel radiances are integrations over the channel filter response functions for each pixel within the 2D image space. Background radiance refers to radiance from the sky, behind the plume; foreground radiance refers to radiance emanating from the atmosphere between the plume and the imager. The foreground and background radiation can be calculated using the MODTRAN-4 radiative transfer model (Berk et al., 1999) using a nearby radiosonde profile for water vapour and temperature and assuming climatological values for the well-mixed gases.

There are other strategies for estimating the effect of the intervening atmosphere between the camera and the target. One possibility is to assume that the atmosphere is locally horizontally and vertically homogeneous and acquire an image (or images) in the opposite direction to the target. Analysis of the brightness temperature images would then provide a background estimate of the atmospheric state without the perturbing influence of the volcanic ash.

"In plume" water vapour is problematic and difficult to estimate. Its effect will be to reduce the signal from volcanic ash, which will lead to underestimates of the ash opacity which will impact also on the retrieval of particle sizes. The overall effect will be an underestimate of the mass of ash in the plume. Without an independent estimate of the "in plume" water vapour it is not possible to eliminate its effect.

The effects of ice may also need to be considered. In the case where the ash plume or cloud is well developed and reaches high into the atmosphere so that ice might be expected to form, the signal from ash may be totally or partially obscured. The ice may be present in such significant amounts that the brightness temperature difference due to ice may swamp that due to ash (ice has the opposite effect to ash on the BTD). The effect will be similar to water vapour and a much reduced estimate of the mass of ash will be obtained. There is also the possibility that ice may encase the ash to an extent that the signal from ash is completely masked by the ice. Prata (1989b) modelled this effect from a satellite viewing perspective, but the result is the same for ground-based viewing: the signal from ice dominates over that from the ash within. In practice we do not expect that ice formation will be a significant occurrence for Cyclops viewing conditions as the most likely orientation will be a low viewing elevation angle (<30°), close (<10 km) to the target volcano. The maximum height observable for a plume emanating at the volcano will be ~6 km, based on Eq. (2). This is generally too low for ice formation.

The detection and retrieval of ash microphysics relies on the thermal contrast between the ash plume and the background. Ideally the background will be the cold sky and the ash plume would be expected to be warmer than the background. It is always possible that a warm cloud, or cloud at a similar temperature to the ash plume, may move behind the ash plume and generate a warm background temperature. The BTD would then decrease and perhaps reach zero or even reverse. The detection algorithm would fail to detect ash. While this could occur it seems unlikely to be common, as the cloud would need to persist and also cover large parts of the field of view for a serious failure of the ash detection algorithm. A more likely situation would be that the detection algorithm would indicate intermittent ash. Clearly the operation of the Cyclops camera needs more testing and operation under a variety of different environmental conditions before the potential failure modes can be properly identified and rectified, if possible. As the preferred mode of operation of Cyclops is continuous and autonomous we have devised a simple statistical-based method to test whether a particular image is likely to indicate ash.

6. Histogram-based alarm

A Cyclops image consists of a maximum of 320×240 pixels, each of which could detect ash. Noise and lack of sensitivity or calibration errors and camera-body temperature fluctuations can also induce anomalous signals into a Cyclops image. In general the structure of these anomalies is very different to that expected from an ash cloud. However, on a pixel-by-pixel basis it is impossible to determine whether the signal is due to a camera anomaly or due to a real ash signature. Analysis of the images obtained from Anatahan volcano (Northern Mariana islands) in conditions where ash was known to be present suggests that the structure in the images can be used to set a threshold or alarm to indicate the presence of ash. To demonstrate how this can be done we first consider a set of Cyclops images obtained in conditions where there was no ash. Fig. 5 shows a brightness temperature difference image (11–12 μm) obtained in ash-free conditions viewing with an elevation of 20° above the horizon. The colour scale on this image indicates a brightness temperature difference range from −15 K to +10 K, with red-coloured pixels having the most positive temperature difference. To highlight the region where most ambiguity might exist, a grey-scale showing temperatures from −0.5 K to +0.5 K is included within the main colour scale. Thus grey-coloured pixels in the temperature difference image may be regarded as marginal, in terms of detectability. In this

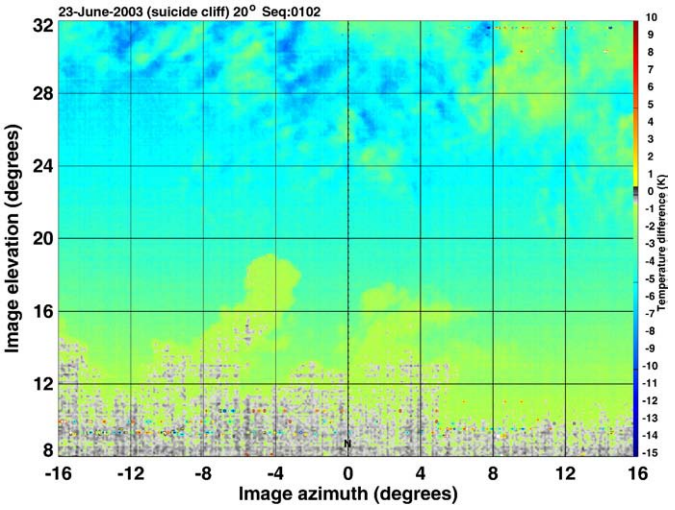

Fig. 5. Cyclops temperature difference image (11–12 μm) obtained at a location (Suicide cliff) on Saipan in the Northern Mariana Islands. The camera elevation was 20° and the camera was viewing to the North (0° azimuth). A colour scale is shown on the extreme right-hand edge of the image; greyed pixels have values from −0.5 to +0.5 K. Nearly all pixels have negative temperature differences, which indicate the scene is composed entirely of clear sky, water vapour and/or mixed phase meteorological clouds.

Please cite this article as: Prata, A.J., Bernardo, C., Retrieval of volcanic ash particle size, mass and optical depth from a ground-based thermal infrared camera, J. Volcanol. Geotherm. Res (2009), doi:10.1016/j.jvolgeores.2009.02.007

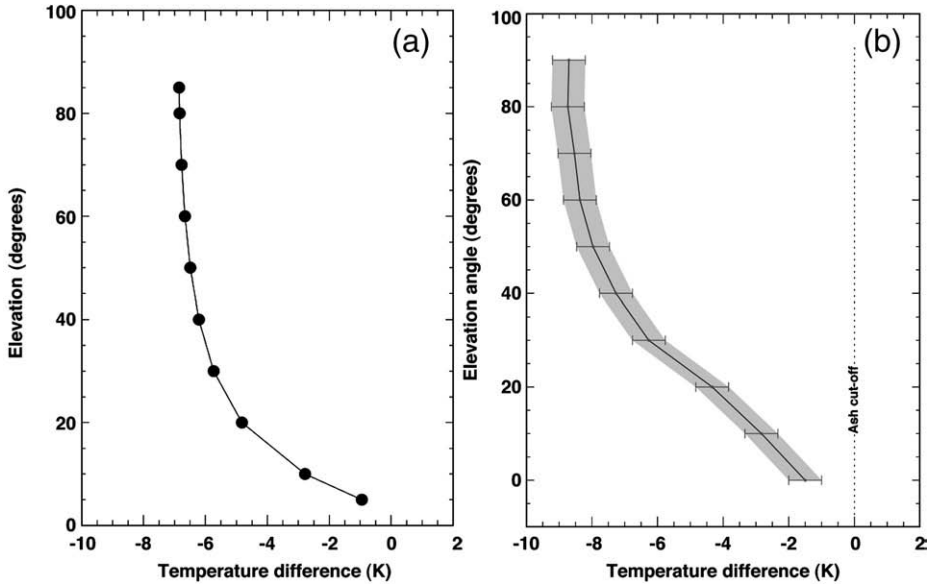

Fig. 6. (a) Variation of elevation angle with temperature difference (11–12 μm) for clear skies determined from radiative transfer modelling. (b) Variation of elevation angle with temperature difference (11–12 μm) for clear skies determined from Cyclops image data. The vertical dashed line shows the theoretical temperature difference value which separates ash affected pixels (pixels to the right of the line) from water vapour, meteorological cloud affected pixels (pixels to the left of the line).

image there are some grey-coloured pixels, but the majority of the pixels are yellow, and green to blue indicating negative temperature differences and hence normal conditions (i.e. clear skies or water/ice meteorological clouds).

From theoretical and modelling calculations we expect pixels that are ash contaminated to have positive differences. But, their actual value depends on viewing conditions, particularly the viewing elevation, and also the amount of water vapour in the path. Theoretical calculations and modelling studies indicate that the difference due to water vapour will be negative when the camera views the sky above the horizon. The exact value of the difference depends on the amount of water vapour, but also on the path length that the radiation traverses through the atmosphere. Fig. 6a shows the variation of the temperature difference (11–12 μm) with elevation for a cloudless atmosphere containing about 3 cm of precipitable water. At low elevation angles the temperature difference is slightly negative, but gets progressively more negative until at around 60° elevation when the difference decreases slowly. Fig. 6b shows the difference as determined from measurements made at Saipan. The variation with elevation angle mimics the theoretical behaviour. These data show more variation than the theoretical studies because the scene also contains clouds and unmodelled water vapour variations. Nevertheless, the temperature difference decreases with elevation angle in all cases studied and agrees with the theoretical behaviour. A consequence of this behaviour is that it is not possible to set a constant threshold for deciding whether Cyclops images contain ash affected pixels.

A threshold value of 0 K for ash is appropriate under most conditions. The image shown in Fig. 5 was obtained at 20° elevation and as the field-of-view of the Cyclops camera is roughly 24° in the vertical direction, some parts of the image view land surfaces. The 2-dimensional histogram of the image is shown in Fig. 7. The same temperature range and colour scale are used for the histogram. The histogram has prominent peaks at roughly temperature differences of −1 K and −5 K which correspond to clouds and clear skies, respectively. In this case the least negative peak has a tail that includes some positive pixels. In the corresponding image these pixels are viewing features that are low on the horizon and include ground targets. Such 'anomalies' are difficult to isolate in an automated manner and could give rise to *false alarms* if a straightforward pixel thresholding technique were employed.

Many such images were acquired at Suicide Cliff, Saipan and at other locations and times (day and night) during the field trials in the Northern Mariana Islands (NMI). The histograms from these images show similar effects on all low elevation images. For some data, anomalies also arise in conditions where there was ash mixed in with significant amounts of water vapour or cloud. In this context these pixels might be considered as important to identify correctly.

The scheme chosen to automatically determine whether an image has detected ash is a statistically based method. This is the method of choice because, by the nature of the problem, there is often going to be a distribution of pixels that can be flagged as ash, within an image

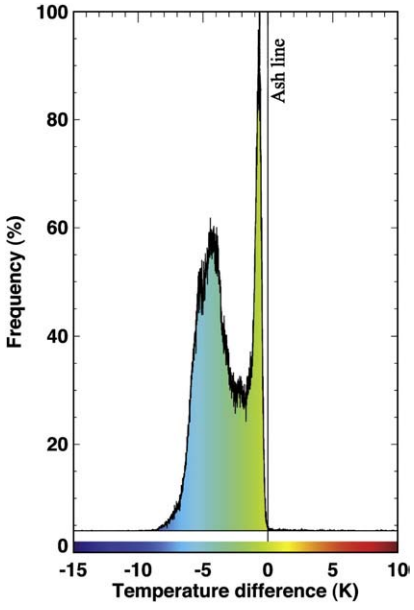

Fig. 7. 2D temperature difference (11–12 μm) image histogram of the data shown in Fig. 4. The ash cut-off line is indicated at 0 K temperature difference. The spread of the histogram is due to a combination of mixed-pixel effects and viewing elevation.

Please cite this article as: Prata, A.J., Bernardo, C., Retrieval of volcanic ash particle size, mass and optical depth from a ground-based thermal infrared camera, J. Volcanol. Geotherm. Res (2009), doi:10.1016/j.jvolgeores.2009.02.007

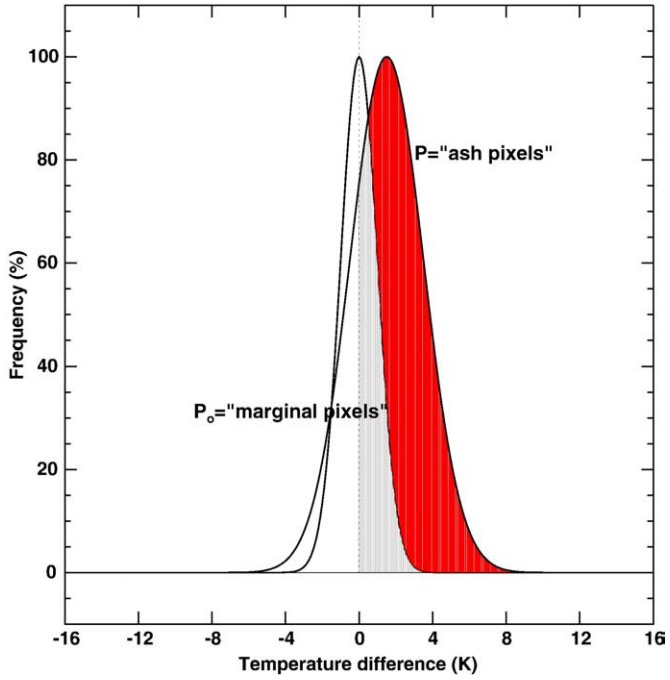

Fig. 8. Illustration of the Gaussian thresholding technique for setting the ash alarm. The grey region contains pixels that fall within the overlap between the *t*-Gaussian; the red-coloured region shows the pixels that are counted as ash affected pixels.

that has many pixels that are definitely ash or definitely not ash. In addition, because of the likelihood that pixels will contain mixtures, a simple threshold and binary decision process would be inappropriate.

6.1. Gaussian fitting

The 2D histogram[2] shown in Fig. 7 consists of two prominent peaks with a spread of pixels around these peaks. If the Cyclops camera viewed a target of constant temperature (e.g. a uniform cloud or the clear sky), then simply because of the fact that the camera has a wide field-of-view and there is water vapour absorption along the differing paths to the target, the resulting difference image would be non-uniform. In practice it is unlikely that the sky would present a uniform target and even less likely that the cloud would be perfectly uniform. The combination of these effects leads to a natural spread in the histogram of the temperature differences, with a central peak corresponding to the mode temperature difference. For a relatively uniform scene, the peak would be high and the spread (or standard deviation of the distribution) would be low. A natural choice to model this kind of distribution is the normal distribution or Gaussian distribution. The Gaussian distribution in mathematical terms is:

$$G(\Delta T) = A_0 exp\left\{-\left(\frac{\Delta T - \mu_{\Delta T}}{\sigma_{\Delta T}}\right)^2\right\}, \quad (8)$$

where ΔT is the temperature difference, $\mu_{\Delta T}$ is the mean temperature difference, $\sigma_{\Delta T}$ is the standard deviation, and A_0 is the maximum frequency, which occurs when $\Delta T = \mu_{\Delta T}$. Each of the peaks ($i = 1 \ldots n$) within the frequency distribution (histogram plot) is assumed to have a mean at $\mu_{\Delta T,i}$ with a spread of $\sigma_{\Delta T,i}$. A set of Gaussian distributions is fitted to the frequency distribution data and the parameters, $A_{0,i}$, $\mu_{\Delta T,i}$, and $\sigma_{\Delta T,i}$ derived. The linear combination of these distributions is the model-fit to the data.

The fit for the histogram data shown in Fig. 7 is shown in Fig. 8. Three Gaussians were used in the fit with parameters given by:

Parameter	$i=1$	$i=2$	$i=3$
$A_{0,i}$	74.2%	24.9%	0.9%
$\mu_{\Delta T,i}$	−4.24 K	−0.84 K	−0.67 K
$\sigma_{\Delta T,i}$	±1.49 K	±0.33 K	±0.08 K

The fit to the distribution although not perfect, is good and can be used for setting the alarm for the image. The alarm technique now proceeds by setting a threshold Gaussian (t-Gaussian) with a mean and standard deviation derived from modelling, and comparing this with the *n*-Gaussian data-fit. The region between the pixels bounded by the *t*-Gaussian mean value, and the overlap region between the two Gaussians (the threshold and the data-fit) is calculated. This area (or number of pixels) is subtracted from the number of pixels that exceed the *t*-Gaussian mean value and lie within the data-fit Gaussian (see Fig. 7). Alarm ratios (in %) are calculated from:

$$R_i = \frac{A_{0,i}}{\sum_{j=1}^{n} A_{o,j}}\left(\frac{P_i - P_{o,i}}{P_i}\right) \quad (9)$$

where $P_{o,i}$ is the number of overlap pixels for Gaussian i, P_i is the number of pixels that exceed the *threshold* mean, and $A_{0,i}$ are the maxima for the Gaussian fits. The purpose of normalising by the maximum is to ensure that more weight is given to distributions that have well-defined and dominant peaks. To demonstrate how the alarm works, we use data obtained from field measurements made at Anatahan volcano (NMI) when viewing an ash cloud and at various locations around Saipan island when viewing clear and cloudy skies (i.e. ash-free conditions). We set thresholds (cut-offs) that depend on viewing elevation and these correspond to the mean of the *t*-Gaussian. The spread or standard deviation of the *t*-Gaussian also depends on elevation angle. Values for these were determined through radiative transfer modelling. Their precise value depends on the atmospheric conditions: principally the amount of water vapour present in the atmosphere.

Fig. 9 shows a histogram obtained in ash-free conditions. There are two prominent peaks (at $\Delta T = -4.24$ K and $\Delta T = -0.84$ K) in the histogram and one minor peak (at $\Delta T = -0.67$ K). The temperature difference in this, and subsequent images corresponds to 11–12 μm temperature differences. A cut-off value of −1.0 K is shown (dashed red line) and the Gaussian-fit (using $n = 3$) is superimposed over the data (green line). In this case the data are represented by three Gaussians. The majority of the pixels (>74%) fall within the Gaussian distribution with mean $\Delta T = -4.24$ K and standard deviation $\sigma_{\Delta T} = \pm 1.49$ K. The *t*-Gaussian for this histogram has a mean of 0 K and a spread of ±2 K. No alarms are generated from these data because none of the pixels in the histogram that lie beyond the cut-off value fall outside the spread of the *t*-Gaussian. No alarm signal would be generated for this image.

A second example is shown in Fig. 10, also obtained in clear/cloudy skies. In this case the camera viewed the scene at a low elevation angle of 10°. Three Gaussians fit the data quite well and the *t*-Gaussian has mean 0 K and standard deviation of ±2 K. In this case the Gaussian that includes most pixels (>94%, $\mu_{\Delta T} = +0.26$ K) generates a 2% alarm. The low alarm is a consequence of the fact that many of the pixels that exceed the cut-off value (0 K) lie within the spread of the *t*-Gaussian and hence are statistically indistinguishable from the expected noise characteristics of the thermal imagery.

A third example is shown in Fig. 11. The imagery in this case was acquired while the camera viewed an ash-laden cloud from Anatahan volcano. Three Gaussian distributions fit the data well. The most significant peak at $\mu_{\Delta T} = +5.45$ K (>91%) generates a 67% alarm. The alarm is less than 91% because some of the pixels within the Gaussian still lie within the spread of the *t*-Gaussian and there are

[2] The use of the terminology 2D histogram is used to signify that the histogram is determined from 2-dimensional spatial domain imagery, as opposed to time-series data or other dimensional data.

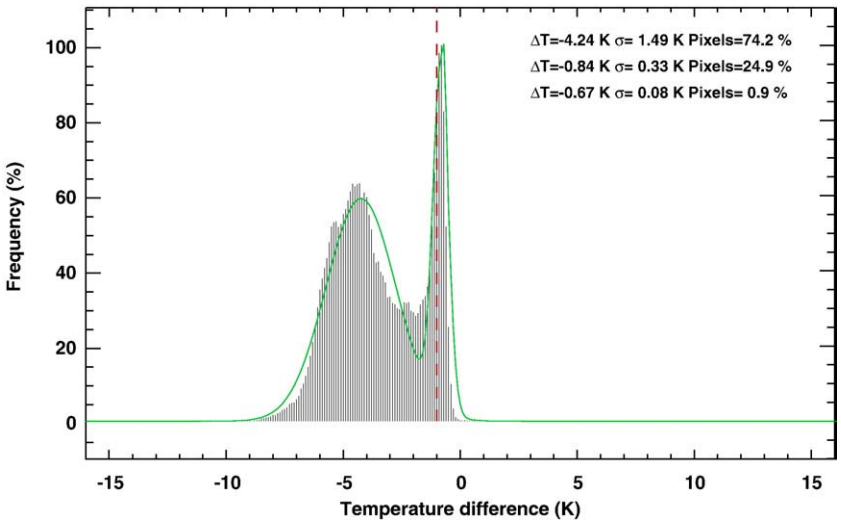

Fig. 9. Gaussian fit to the histogram data obtained from Suicide Cliff on 23-June, 2003. Also shown is the *t*-Gaussian and the decision of whether an alarm is indicated or not.

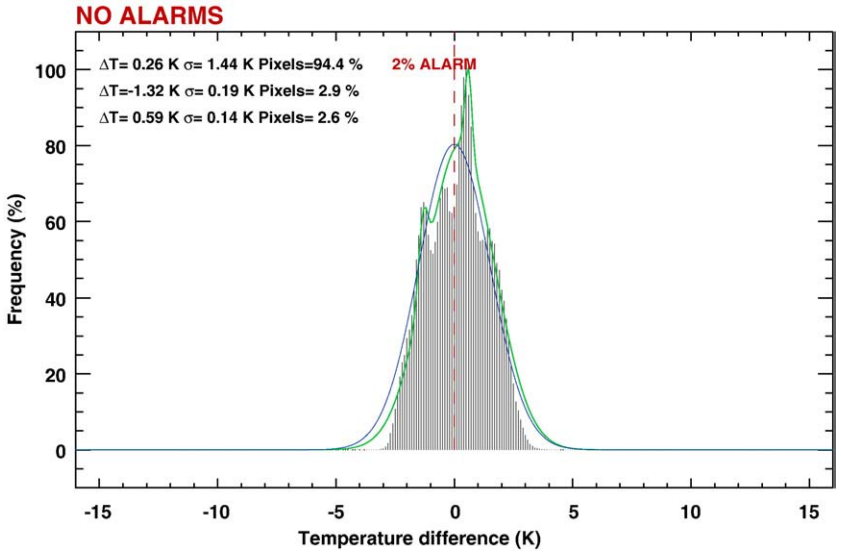

Fig. 10. Gaussian fit to the histogram data obtained when viewing clear skies near Anatahan volcano.

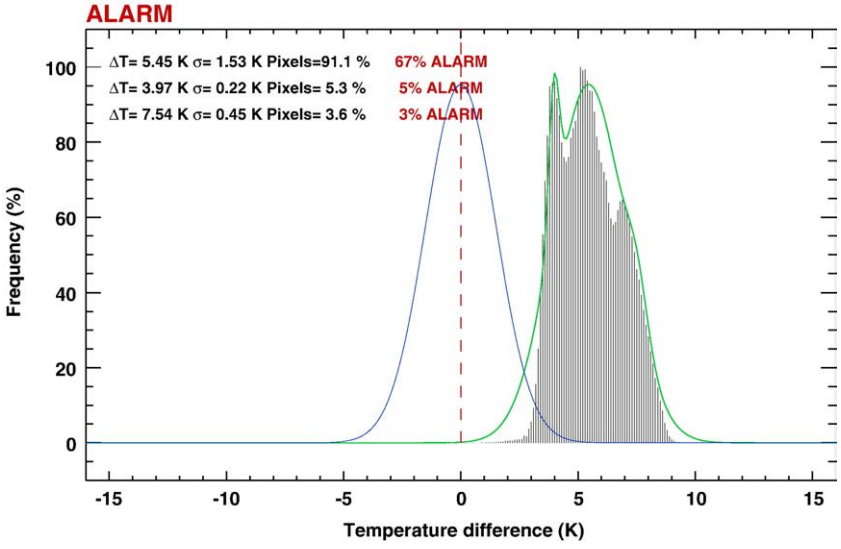

Fig. 11. Gaussian fit to the histogram data obtained when viewing an ash cloud from Anatahan volcano, Northern Mariana Islands.

Please cite this article as: Prata, A.J., Bernardo, C., Retrieval of volcanic ash particle size, mass and optical depth from a ground-based thermal infrared camera, J. Volcanol. Geotherm. Res (2009), doi:10.1016/j.jvolgeores.2009.02.007

≈10% of the pixels included within the second and third Gaussians. The automated ash alarm algorithm is a useful qualitative tool for fast processing and communication of information to indicate the presence of ash within the field of view of the camera. Quantitative analyses are also possible, and a more sophisticated retrieval scheme has been developed and is described in the next Section.

7. Ash microphysical retrievals

Volcanic ash contains SiO_2 in varying amounts. Basaltic ash contains the least (<50%) followed by andesitic, dacitic and rhyolitic ash contains the most SiO_2 (>60%). Sarna-Wojcicki et al. (1981) describe many aspects of volcanic ash and Baxter (1999) discusses the microphysics of ash relevant to health impacts. A few measurements of the sizes and size distributions of airborne ash particles have been made (Chuan et al., 1981; Hobbs et al., 1981) and these suggest that particles in the range 1–10 μm (radii) are common. Larger particles tend to fall out quickly and smaller ones coagulate causing an atmospheric sieving effect that leaves the majority of particles in a size range amenable to remote sensing by utilizing infrared radiation near 10 μm. Smaller particles ($r<1$ μm) and larger particles ($r>10$ μm) are likely to be present but these are of less interest here, where the focus is on particles that can remain in the atmosphere to present a hazard to aviation and a concern for public health. These two main observations regarding volcanic ash, viz. the high SiO_2 content and typical particle sizes in the 1–10 μm range, strongly suggest that the infrared region between 8–14 μm is useful for retrieving ash microphysics.

A discrete ordinates radiative transfer model (e.g. Stamnes and Swanson, 1981; Prata, 1989b) was used together with optical properties of silicate particles to simulate temperatures for the Cyclops bands and viewing conditions. A large number of calculations were performed to encompass a range of conditions. The calculations provide temperatures as a function of particle radius (r), infrared optical depth (τ), and zenith viewing angle (θ) for a volcanic cloud with uniform temperature T_c and a background temperature T_b. It is unlikely that the size distribution of particles in an ash cloud is uniform, so a modified γ-distribution (King et al., 1984; Hofmann and Rosen, 1984) is used in the radiative transfer calculations. This distribution has been used previously in simulating satellite measurements for volcanic clouds (Prata, 1989b; Wen and Rose, 1994; Prata and Grant, 2001). A three-dimensional data cube with axes, r, τ, θ is derived for scene temperatures T_c and T_b. The data cube is used to perform a retrieval starting from Cyclops temperature measurements and viewing geometry ending with the microphysical variables, r and τ. The $r\tau\theta$ data cube is searched along the planes corresponding to constant values of T_i, $\Delta T_{i,j}$ and θ. These planes intersect at solution values of r^*, τ^* and θ^*, which occur when the difference between calculated and measured T_i and $\Delta_{i,j}$ are a minimum. The microphysical retrieval may be represented by:

$$\mathcal{R}(r,\tau,\theta;M) \leftarrow \mathcal{G}\left(T_i,\Delta T_{i,j},\theta;P\right). \tag{10}$$

P includes the physical constraints supplied by the microphysical model (viz. size distribution, real and imaginary refractive indices, density of ash) and ensures that the problem is well-posed. The symbol ← represents an interpolation between the data cube (G) and the $r\tau\theta$ cube (R). Retrievals are terminated in the limit of high optical depth $\tau>4$ or in cases where $\Delta T_{i,j} \geq \Delta T_{\text{cut}}$, with ΔT_{cut} set arbitrarily between values of 0 to −2 K, depending on background atmospheric conditions. When atmospheric corrections are applied, exactly the same procedure is used but with atmospherically corrected brightness temperatures and a 0 K cut-off.

Given that there are many assumptions and approximations involved in the retrievals, it is sensible to use integrated quantities that smooth out errors. A variable of some interest for both the ash hazard and for understanding volcanic eruption processes is the mass of fine ash erupted. The number of particles per unit volume in the cloud is:

$$N = \int_o^\infty \frac{dn(r)}{dr} dr, \tag{11}$$

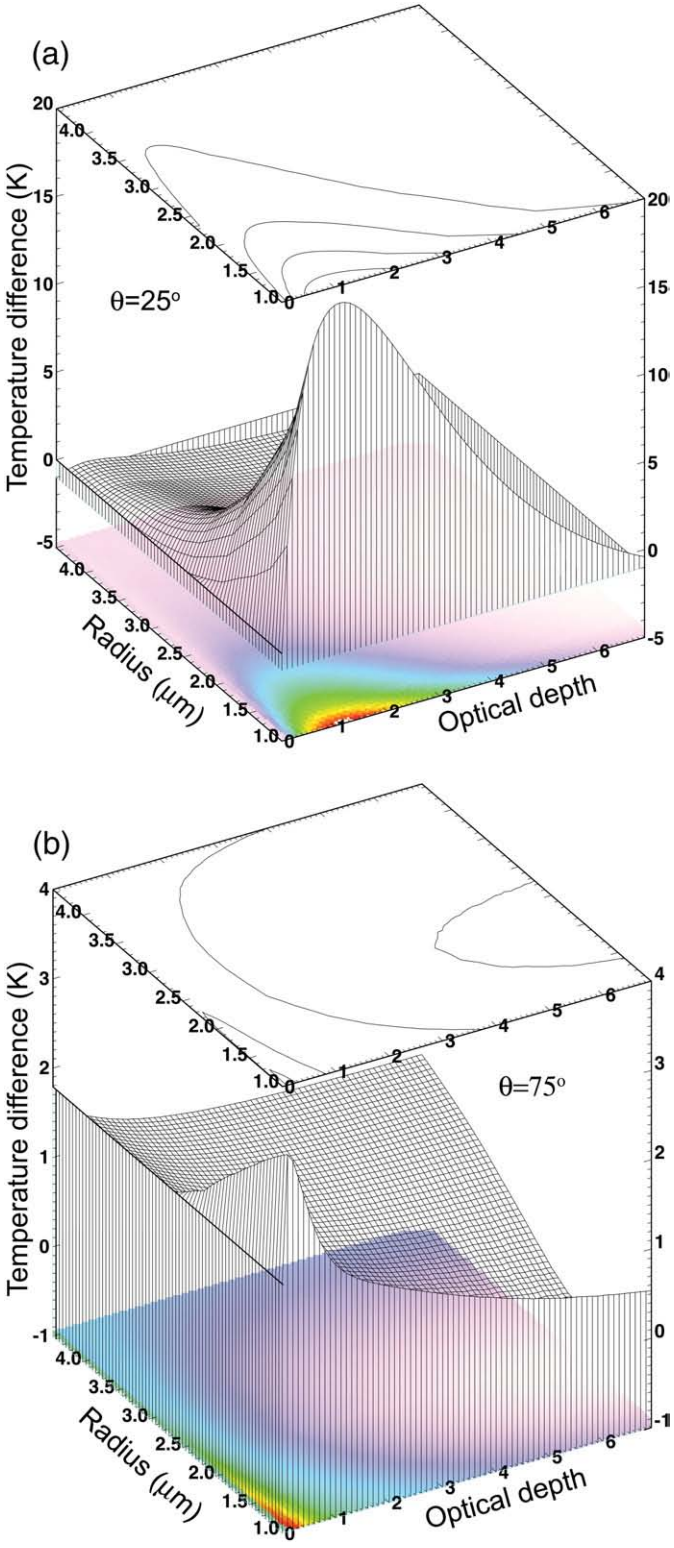

Fig. 12. (a) The temperature difference, particle radius, and optical depth retrieval space for a viewing zenith angle of 25°. The solution is found by finding the intersection between the temperature difference and the radius-optical depth surface. In most cases this is a well-defined problem and the intersection point is unique. (b) As for (a) but for a viewing zenith of 75°.

Please cite this article as: Prata, A.J., Bernardo, C., Retrieval of volcanic ash particle size, mass and optical depth from a ground-based thermal infrared camera, J. Volcanol. Geotherm. Res (2009), doi:10.1016/j.jvolgeores.2009.02.007

Fig. 13. Photograph of the Cyclops camera viewing an eruption column from Tavurvur, Rabaul, New Britain. The camera is approximately 7 km from the erupting volcano.

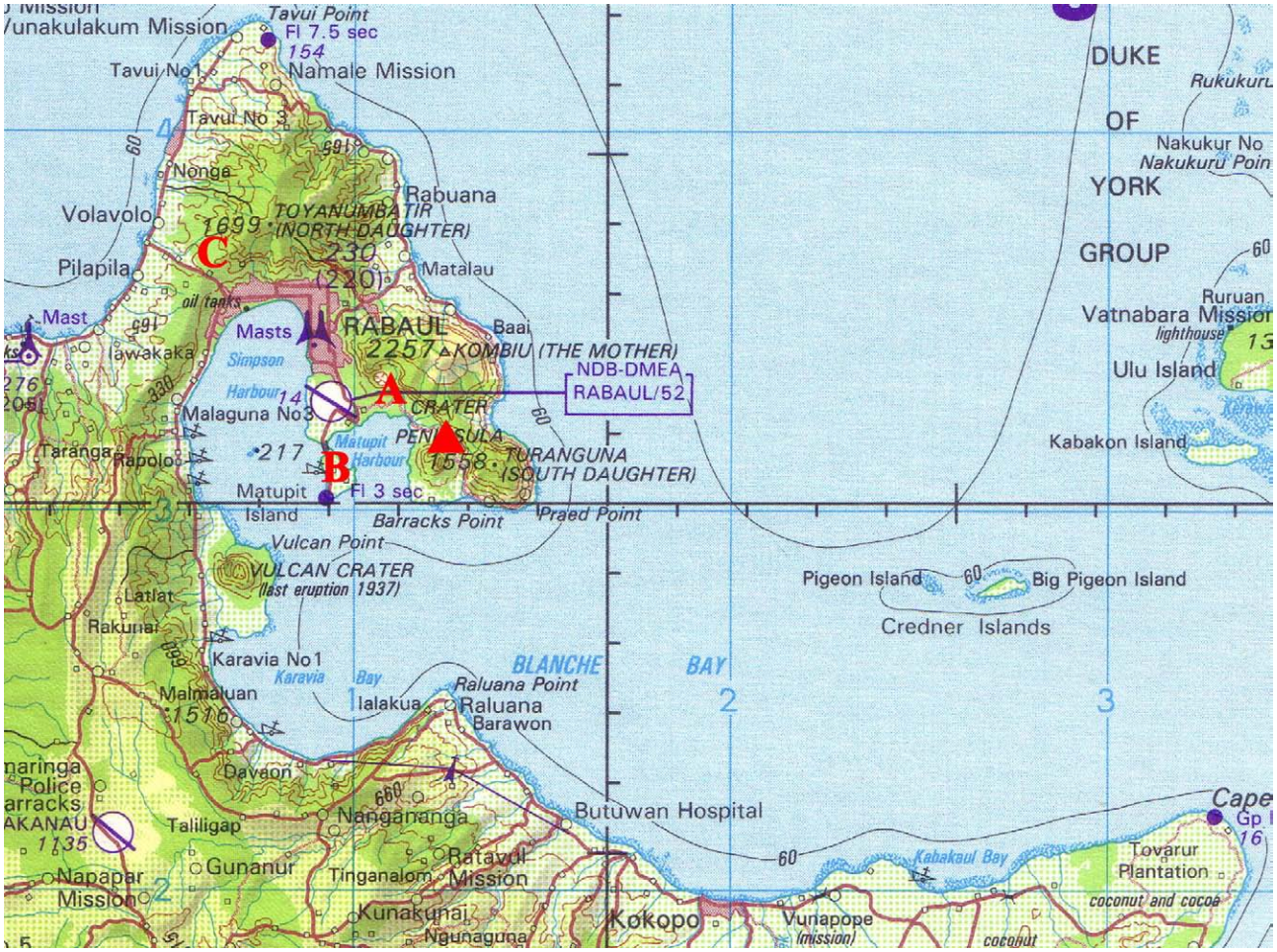

Fig. 14. Map of Rabaul, New Britain showing the locations of Cyclops measurements. A is on the beach at Rababa, B is at Matupit village and C is at the Rabaul Volcanological Observatory (RVO). The location of the erupting crater is indicated by the red-coloured triangle. This map shows the location of the airport that was destroyed in the 1994 eruption. The new airport (not marked) is now located on the eastern part of New Britain, near Kokopo and much further from the volcano.

Please cite this article as: Prata, A.J., Bernardo, C., Retrieval of volcanic ash particle size, mass and optical depth from a ground-based thermal infrared camera, J. Volcanol. Geotherm. Res (2009), doi:10.1016/j.jvolgeores.2009.02.007

Fig. 15. Photograph of Cyclops at Rababa "hot springs" during a measurement sequence and nearly continuous ash eruption activity.

where $n(r)$ is the (assumed) size distribution and the optical depth of the cloud is:

$$\tau_\lambda = \pi L \int_o^\infty r^2 Q_{\text{ext}}(r, \lambda) n(r) dr, \tag{12}$$

L is the geometrical thickness of the cloud. The polydisperse extinction efficiency (Q_{ext}) is:

$$\hat{Q}_{\text{ext}} = \frac{\int_o^\infty \pi r^2 Q_{\text{ext}}\left(\frac{2\pi r}{\lambda}, m\right) \frac{dn(r)}{dr} dr}{\int_o^\infty \pi r^2 \frac{dn(r)}{dr} dr}. \tag{13}$$

The mass loading of fine ash (kg m^{-3}) is:

$$m_l = \frac{4\pi}{3} \rho \int_o^\infty r^3 n(r) dr, \tag{14}$$

where ρ is the density of the ash. The total mass M (in kg) can be evaluated by summing over all affected image pixels using the retrievals of r and τ and multiplying by the area, A_p of a pixel:

$$M = \sum_p A_p \frac{4\pi}{3} r_p \tau_p \frac{\int_o^\infty \pi r^2 n(r) dr}{\int_o^\infty \pi r^2 Q_{\text{ext}}(r, \lambda) n(r) dr} \tag{15}$$

Examples of the $r\tau\theta$ retrievals are shown in Fig. 12a,b, for $T_v = 295$ K, $T_b = 230$ K, $T_i = T(10\ \mu\text{m channel})$ and $T_j = T(12\ \mu\text{m channel})$. Each panel shows a slice through the θ-plane:- top panel shows $\theta = 25°$ and bottom panel $\theta = 75°$. At low zenith angles (high elevation angles) positive temperature differences are apparent for optical depths up to 4 and particle radii in the range $1 \le r \le 4$ μm. As the zenith angle increases, pathlengths increase and positive temperatures only occur for low optical depths and small particles, $r \approx 1$ μm. In this case, the denser ash cloud becomes opaque to infrared radiation and the emissivity effect dominates over scattering and absorption of radiation. There are two possible routes to the high opacity limit; either through a combination of numerous small

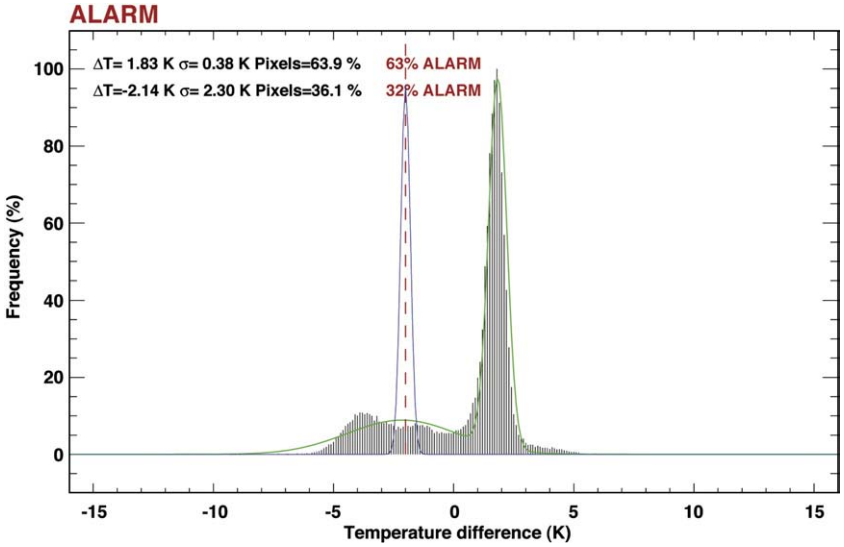

Fig. 16. 2D temperature difference (11–12 μm) histogram obtained at Rababa "hot springs" when the atmosphere was ash-laden. A low threshold (−2 K) was used for the ash cut-off because the background atmosphere also contained ash. In this case the automated alarm algorithm, indicates that 64% of the pixels are ash affected.

Please cite this article as: Prata, A.J., Bernardo, C., Retrieval of volcanic ash particle size, mass and optical depth from a ground-based thermal infrared camera, J. Volcanol. Geotherm. Res (2009), doi:10.1016/j.jvolgeores.2009.02.007

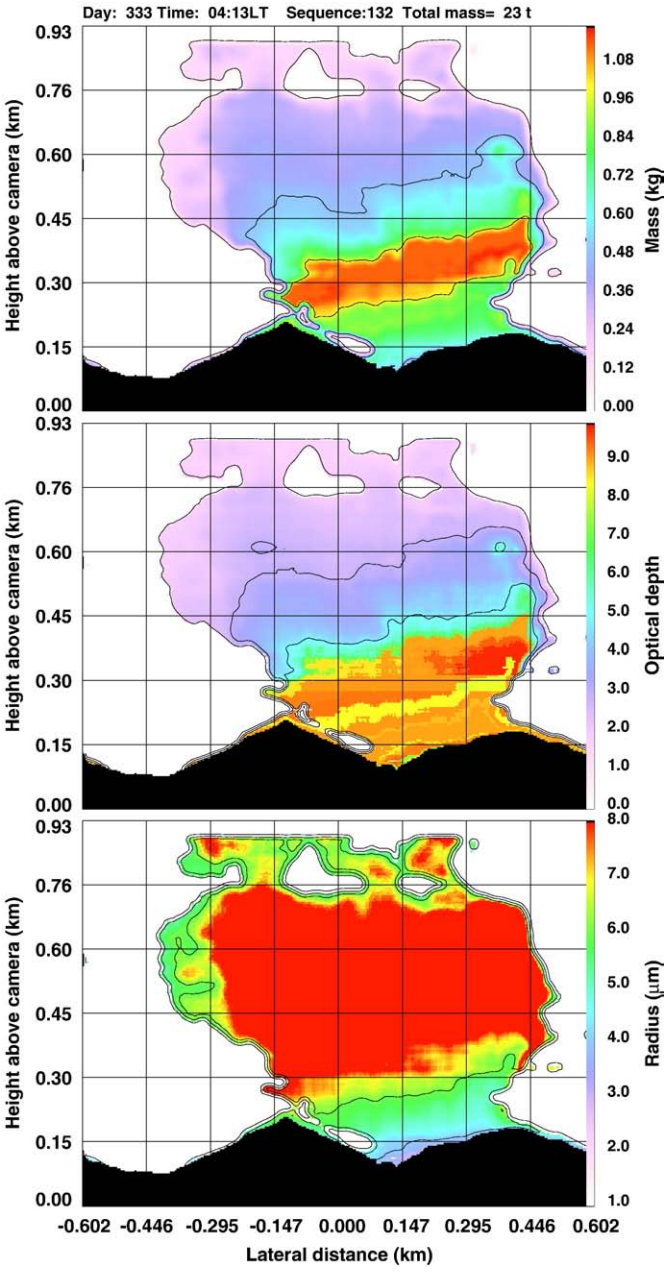

Fig. 17. Mass (kg), infrared optical depth (dimensionless) and particle radius (μm) retrievals for measurements made from Rababa, Rabaul, New Britain. Top panel: mass. Middle panel: optical depth. Bottom panel: particle radius. The image coordinates are height above the camera (km) and lateral distance (km) relative to the centre of the camera.

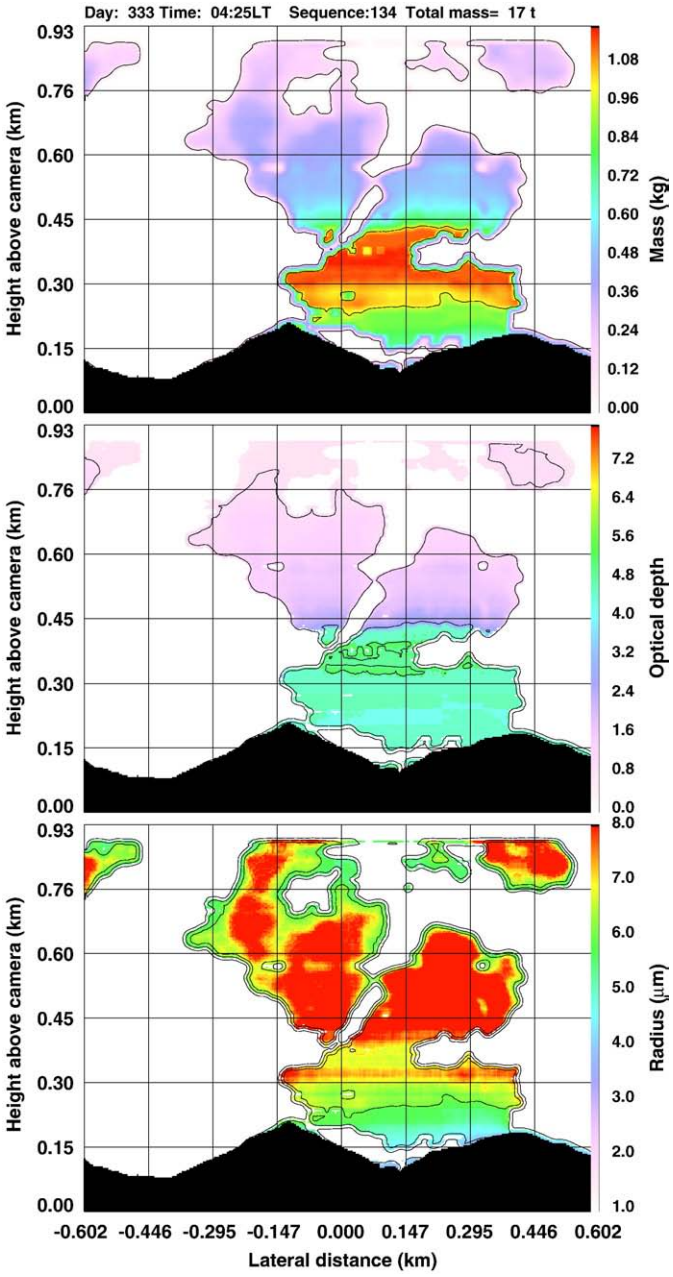

Fig. 18. As for Fig. 17 but about 12 min later, showing the break-up and dispersion of the ash column.

particles and long geometrical path lengths, or through massive particles and shorter pathlengths. Since silicates have a lower emissivity at 10 μm than at 12 μm, temperature differences are always negative, regardless of the temperature of the ash and background, once the cloud becomes opaque.

8. Results: measurements at Tavurvur, Rabaul, PNG

A series of tests were conducted at Tavurvur volcano, near the town of Rabaul on New Britain. A large eruption occurred here on 19 September 1994 and since then the volcano has had near-continuous activity, including week-long periods of small-sized (column heights to 1–3 km) ash eruptions every 20–60 min. During the experimental period, ash eruptions were observed frequently; small explosive events occurring as often as every few minutes, and the air was often ash-laden. Measurements were made from several locations, with varying line-of-sight distances from the crater and varying viewing angles were employed. A photograph (Fig. 13) taken from the Rabaul Volcanological Observatory (RVO) approximately 7 km away, shows one of the many small-sized eruptions observed by Cyclops. Measurements were acquired from the locations shown on the map in Fig. 14. Results are presented for three locations: at the Rababa "hot springs" site (A), from Matupit village (B) and from RVO (C).

8.1. Rababa

This site was very close to the eruption crater (<1 km), and although emissions were not continuous, explosions were frequent enough to ensure that the sky was constantly filled with ash. This meant that absorption would be strong and perhaps make ash discrimination difficult. Fig. 15 shows the Cyclops camera on the beach

Please cite this article as: Prata, A.J., Bernardo, C., Retrieval of volcanic ash particle size, mass and optical depth from a ground-based thermal infrared camera, J. Volcanol. Geotherm. Res (2009), doi:10.1016/j.jvolgeores.2009.02.007

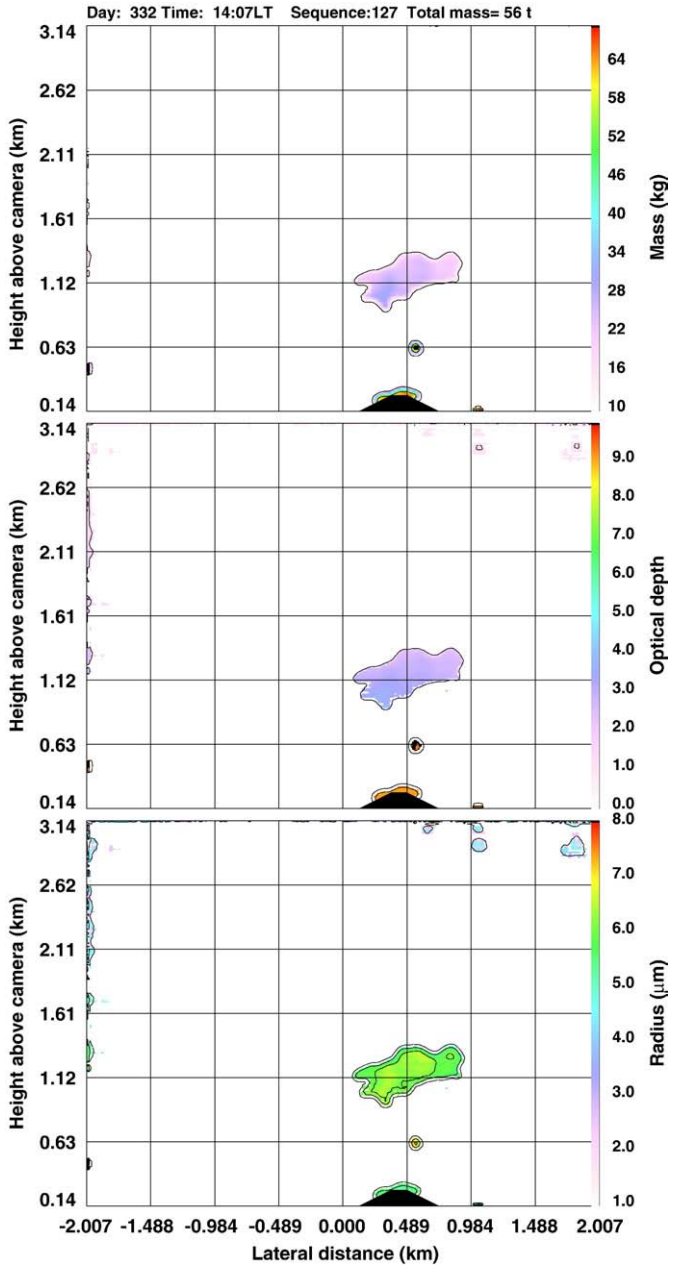

Fig. 19. Mass (kg), infrared optical depth (dimensionless) and particle radius (μm) retrievals for measurements made from Matupit village, Rabaul, New Britain. Top panel: mass. Middle panel: optical depth. Bottom panel: particle radius. The tip of the volcano is indicated in black using a mask generated by temperature thresholding the broadband Cyclops image data.

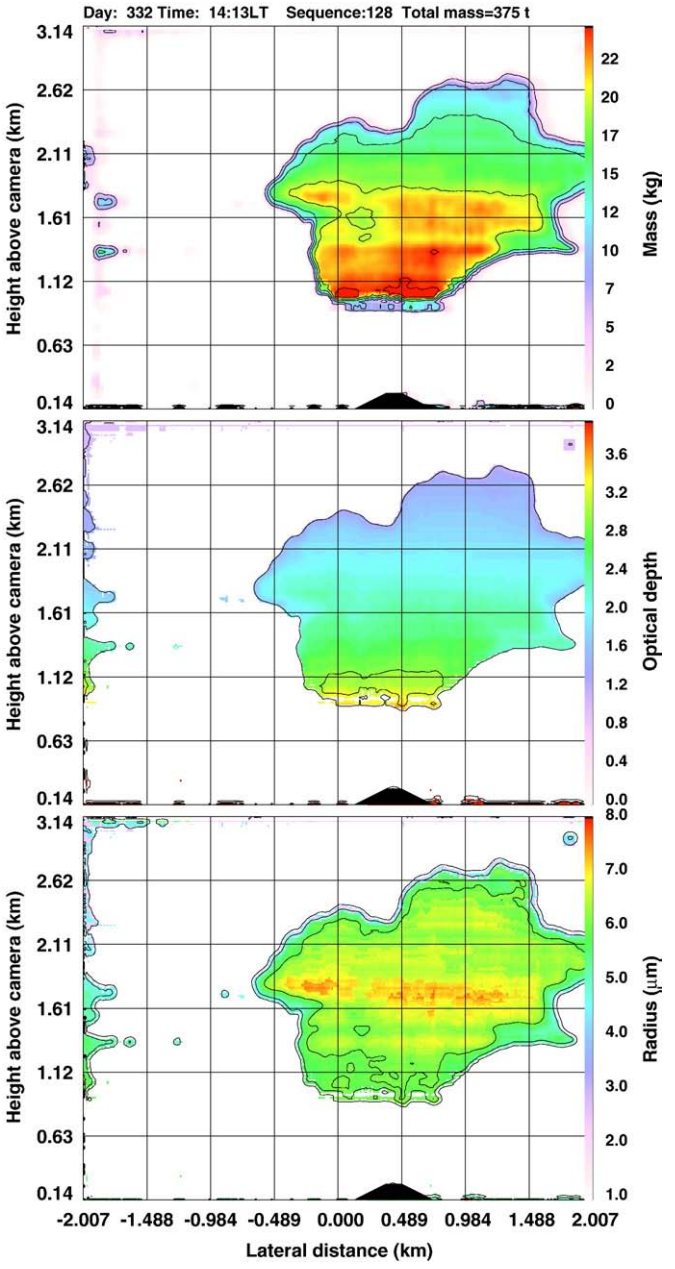

Fig. 20. As for Fig. 19 but 5 min later.

opposite Tavurvur making automated measurements during a period of almost continuous eruptive activity. An alarm histogram for a measurement sequence taken at Rababa beach is shown in Fig. 16, where the alarm threshold has been set at −2 K. This is quite a low threshold and was required because there was so much ash in the sky that the camera was operating inside the ash cloud at high optical depths.

Particle microphysics retrievals were made from data acquired at this site. The proximity of the camera to the erupting ash cloud inevitably meant that the camera was inside the plume during measurements. Retrievals are shown for two sequences separated by about 11 min in Figs. 17 and 18. Each figure contains three panels: the top panel shows the mass of fine ash in the cloud (in kg), the middle panel shows the optical depth, and the bottom panel shows the mean effective particle radius (in μm). The development of the ash column can be traced in the retrieval products, with most mass at the base of the column at the start of the eruption and ascending in usually a vertically layered structure as time progresses. The total mass of the cloud is calculated by summing the masses of individual pixels contained within the image, and is indicated at the top of each figure. No compensation is made for ash that moves out of the field-of-view of the camera. Ash particles within the fine range size do not seem to show vertical stratification, rather the main structure suggests smallest particles exist at the periphery of the cloud and largest particles remain within the central portion. The interplay of the internal dynamics of the developing ash column, gravitational effects and the environmental wind field lead to a varied and complex 3D particle distribution in these weakly erupting ash columns, making meaningful conclusions difficult. However, these initial results are indicative of the kind of analyses that could be performed if faster sampling and perhaps multiple cameras were available.

Please cite this article as: Prata, A.J., Bernardo, C., Retrieval of volcanic ash particle size, mass and optical depth from a ground-based thermal infrared camera, J. Volcanol. Geotherm. Res (2009), doi:10.1016/j.jvolgeores.2009.02.007

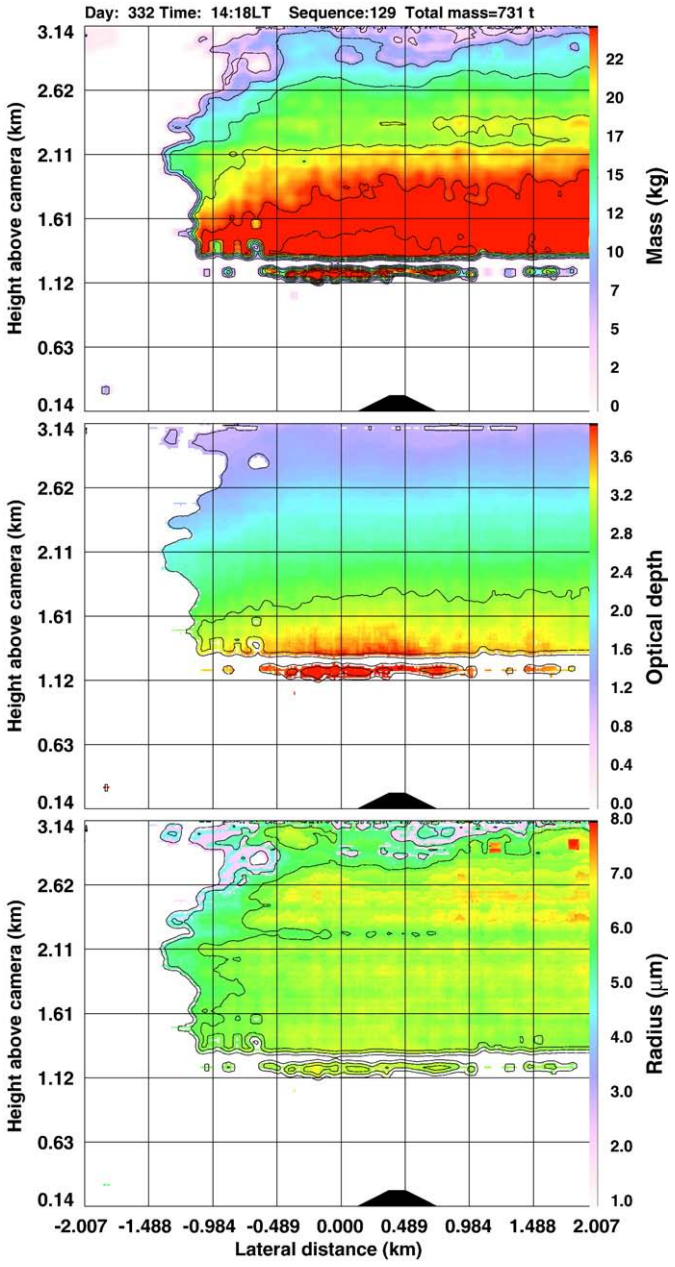

Fig. 21. As for Fig. 20 but 5 min later.

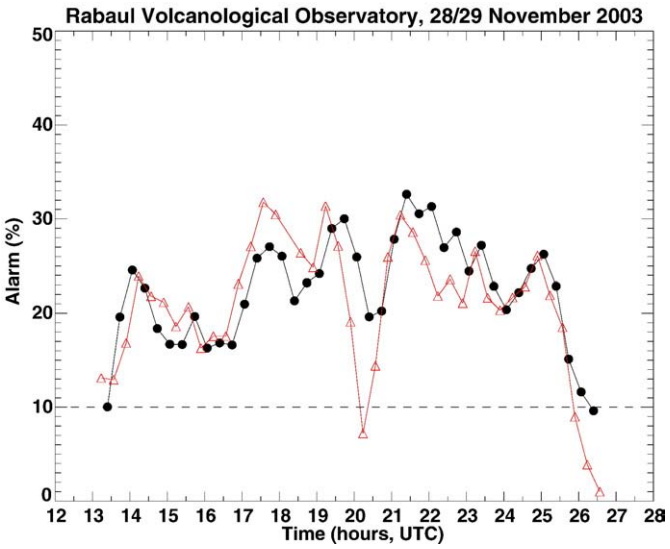

Fig. 22. Time-series of Cyclops image alarms obtained over a period of ~12 h while the Cyclops camera was viewing Tavurvur volcano, from Rabaul Volcanological Observatory about ~7 km distant. Two series of measurements are shown, each point is separated by ~5 min. During the period, activity was high enough to trigger the alarm most of the time.

8.2. Matupit village

This site and another location nearby were chosen because they were further from the crater (2–3 km) and allowed a view to the ash plume from a position outside the main ash affected atmosphere. A sequence of three retrievals is shown in Figs. 19–21.The retrievals are separated in time by about 5–6 min, and these were acquired during the day. The top of the crater is shown pictorially in black on each panel and some smoothing has been applied to the retrievals. The sampling rate is not sufficient to allow individual cloud puffs to be tracked, but there is consistency of the development of the ash cloud as it exits the crater and ascends and expands into the atmosphere. As before the total mass is calculated and shown at the top of each retrieval.

It is useful to determine mass loadings (kg m^{-3}). This could be done quite well by using three cameras simultaneously to properly constrain the geometry of the developing ash cloud. However, only one camera was available and an alternate method for estimating the volume of the cloud is needed. By idealising the shape of the cloud as an inverted circular frustum (truncated cone) an estimate, albeit crude, of the volume of the cloud can be made. Using these volume estimates, the mass loadings for these retrievals is found to vary from ~500 mg m^{-3} at the start of an eruption event (Fig. 18) to ~30 mg m^{-3} after 15 min (Fig. 20). These values are well in excess of the recommended exposure limits of 1 mg m^{-3}.

8.3. RVO

The final location chosen for testing the Cyclops camera was on a hill ~7 km from Tavurvur at the site of the Rabaul Volcanological Observatory. The main reason for selecting this site was to test whether the camera could operate in a fully autonomous mode, providing ash alarms with the purpose of alerting the relevant authorities of the presence of ash in the atmosphere. At this distance and orientation (see Fig. 12) the camera is able to image a large portion of the atmosphere around the erupting crater and also measure quite tall columns (several kilometers). The *t*-Gaussian automated procedure was used to obtain ash alarms and results for a period of about 12 h (over-night) are shown in Fig. 22. In this plot, data were divided into two separate time-series, each series with 10 min samples, and indicated by red triangles and black circles. This was done simply to investigate appropriate sampling rates and to check on the consistency of the automated alarm system. The dashed line is an arbitrarily set threshold of 10%. Throughout the night and into the morning, ash was detected by Cyclops at levels high enough to be of concern. There is a noticeable dip in the ash amount at around 20:00UTC (Local time = UTC + 10), which is detected in both time series. Later analysis of the image data shows that this was in fact a reduction in the activity of the volcano, but it could equally have been due to a change in the wind direction, taking ash away from the viewing direction of the camera. This effect would be greatest when the wind takes the plume away from the camera and in a direction that is parallel to the viewing direction of the camera. If local wind information is also available while the camera is operating, it might be possible to isolate wind effects from changes in volcanic activity. It is also possible to link traditional volcanological measurements (e.g. seismic data) with the camera output to provide greater confidence in the ash alarm system.

Please cite this article as: Prata, A.J., Bernardo, C., Retrieval of volcanic ash particle size, mass and optical depth from a ground-based thermal infrared camera, J. Volcanol. Geotherm. Res (2009), doi:10.1016/j.jvolgeores.2009.02.007

9. Conclusions

This paper reports the first measurements of microphysical properties of airborne ash from an innovative thermal imaging camera system. A detailed description of the two operating modes of the system has been given. These modes are intended for different users and uses. Mode 1 provides an automated alarm obtained by operating the camera unattended and utilising a completely automatic algorithm, which requires little interpretation. This mode is intended for use at airports, volcanological observatories or in cities affected by airborne volcanic ash. Users of this operating mode can couple other kinds of data to the system to improve confidence or remove ambiguities in interpretation of volcanic activity. For example, wind information, seismic data, satellite measurements (e.g. Schneider et al., 1995), or ultra-violet spectrometer measurements (Galle et al., 2002) could be coupled with the system. Mode 2 operation of the camera provides microphysical retrievals of mass, particle radius and infrared optical depth-data that can be used for assessing risk levels from ash, for volcanological research and for developing models of the dynamics and behaviour of developing eruption columns and plumes.

While proof-of-concept and successful testing of the system have now been demonstrated, several limitations of the current system have been found. The most serious of these is the size of the temperature noise (NEΔT) of the microbolometer array. Broadband noise levels of NEΔT ~ 50 mK are currently achievable, but this rises to up to 200 mK for narrowband filtered radiation at low temperatures. With improvements in technology the NEΔT′s will decrease in the future. Another limitation of the current system is the slowness of acquiring image data from the camera. This is only a limitation of the current system and by using a faster communication protocol and electronics, this limitation is easily overcome. After allowing for some time to calibrate and acquire up to 5 channels of filtered image data (a sequence), sampling rates of one sequence per minute are achievable. At this rate it is possible to explore the dynamics of eruption columns and plumes and even track features in consecutive image sequences. If three such cameras could be deployed at one site in a carefully designed viewing orientation, it would be possible to have a highly sophisticated fully autonomous ash alarm system offering research standard 4-dimensional (3 space and time) data. Such systems could be deployed near to volcanoes that are close to airports where the threat of disruption by ash-fall may be significant (Guffanti et al., in press).

The kind of system suggested here is most appropriate for Rabaul, where a troublesome volcano continues to disrupt the community and cause problems with air transport to and from the island. The eruption of 1994 destroyed the main airport, which has now been moved to Kokopo (see the map in Fig. 14). This new airport is not under direct threat from an eruption of Tavurvur, but ash drifting into the path of air traffic or falling on the runway is very disruptive, and can cause the airport′s closure. Currently no early warning of ash in the atmosphere is available in New Britain. The system is also appropriate for deployment at population centres and airports under direct threat from volcanic ash eruptions or suffering on-going ash eruptions.

Acknowledgments

We thank the two anonymous reviewers for their helpful comments and suggestions. This work was started while both authors were with the CSIRO, Australia. Lack of foresight and changed priorities caused the closure of the research program. We are most grateful to the Norwegian Institute for Air Research and Auspace Ltd. for allowing us to complete this innovative and useful research and development.

References

Baxter, P.J., 1999. Impacts of eruptions on human health. In: Siggurdson, H. (Ed.), Encyclopaedia of Volcanoes. Academic Press, New York, pp. 1035–1043.
Berk, A., Anderson, G.P., Bernstein, L.S., Acharya, P.K., Dothe, H., Matthew, M.W., Adler-Golden, S.M., Chetwynd Jr., J.H., Richtsmeier, S.C., Pukall, B., Allred, C.L., Jeong, L.S., Hoke, M.L., 1999. MODTRAN4 radiative transfer modeling for atmospheric correction. SPIE Proceeding, Optical Spectroscopic Techniques and Instrumentation for Atmospheric and Space Research III, p. 3756.
Bernardo, C., Prata, A.J., 2008. Calibration of a microbolometer array filter radiometer Submitted to Applied Optics.
Casadevall, T.J., 1994. The 1989/1990 eruption of Redoubt Volcano Alaska: impacts on aircraft operations. J. Volcanol. Geotherm. Res 62 (30), 301–316.
Casadevall, T.J., Delos Reyes, P.J., Schneider, D.J., 1996. The 1991 Pinatubo eruptions and their effects on aircraft operations. In: Newhall, C.G., Punongbayan, R.S. (Eds.), Fire and Mud: eruptions and lahars of Mount Pinatubo, Philippines, 625–636, Quezon City: Philippines Institute of Volcanology and Seismology. University of Washington Press, Seattle.
Chahine, M.A.T., Pagano, T.S., Aumann, H.H., et al., 2006. AIRS: improving weather forecasting and providing new data on greenhouse gases. Bull. Amer. Meteorol. Soc. 910–926. doi:10.1175/BAMS-87-7-911.
Chuan, R.L., Woods, D.C., McCormick, M.P., 1981. Characterisation of aerosols from eruptions of Mount St. Helens. Science 211, 830–832.
Galle, B., Oppenheimer, C., Geyer, A., McGonigle, A.J.S., Edmonds, M., Horrocks, L., 2002. A miniaturised ultraviolet spectrometer for remote sensing of SO_2 fluxes: a new tool for volcano surveillance. J. Volcanol. Geotherm. Res. 119, 241–254.
Guffanti, M., Mayberry, G.C., Casadevall, T.J., Wunderman, R., 2008. Nat. Hazards. doi:10.1007/s11069-D08-9254-2..
Hobbs, P.V., Radke, L.F., Eltgroth, M.W., Hegg, D.A., 1981. Airbome studies of the emissions from the volcanic eruptions of Mount St. Helens. Science 211, 816–818.
Hofmann, D.J., Rosen, J.M., 1984. Balloon-borne particle counter observations of the El Chichón aerosol layers in the 0.01–1.8 μm radius range. Geofis. Int. 23, 155–185.
Huang, H.L., Yang, P., Wei, H., Baum, B.A., Hu, Y., Antonelli, P., Ackerman, S., 2004. Inference of ice cloud properties from high spectral resolution infrared observations. IEEE Trans. Geosci. Remote Sens. 42 (4), 842–853.
King, M.D., Harshvardhan, Arking, A., 1984. A model of the radiative properties of the El Chichón stratospheric layer. J. Climate Appl. Meteorol. 23, 1121–1137.
Kruse, P.W., 2001. Uncooled Thermal Imaging: Arrays, Systems, and Applications, vol. TT51. SPIE Press, Bellingham, Washington, p. 90.
Lamb, H.H., 1970. Volcanic dust in the atmosphere; with a chronology and assessment of its meteorological significance. Philos. Trans. R. Soc. Lond. Ser. A 266, 425–533.
Prata, A.J., 1989a. Observations of volcanic ash clouds using AVHRR-2 radiances. Int. J. Remote Sens. 10 (4–5), 751–761.
Prata, A.J., 1989b. Radiative transfer calculations for volcanic ash clouds. Geophys. Res. Lett. 16 (11), 1293–1296.
Prata, A.J., Barton, I.J., 1993. Detection and discrimination of volcanic ash clouds by infrared radiometry I. In: Casadevall, T. (Ed.), Theory, International Symposium on Volcanic Ash and Aviation Safety. USGS.
Prata, A.J., Grant, I.F., 2001. Retrieval of microphysical and morphological properties of volcanic ash plumes from satellite data: application to Mt. Ruapehu, New Zealand. Quart. J. Roy. Meteorol. Soc. 127 (576B), 2153–2179.
Prata, A.J., Bernardo, C., submitted for publication. Retrieval of SO_2 from a ground-based thermal infrared imaging camera system, Submitted to J. Geophys. Res.
Robock, A., 2000. Volcanic eruptions and climate. Rev. Geophys. 38 (2), 191–219.
Robock, A., Mass, C., 1982. The Mt. St. Helen's volcanic eruption of 18 May 1980: large short-term surface temperature effects. Science 216, 628–630.
Sarna-Wojcicki, A.M., Shipley, S., Waitt, R.B., Dzurisin, D., Wood, S.H., 1981. Areal distribution, thickness, mass, volume, and grain size of air-fall ash from six major eruptions of 1980. In: Lipman, Peter W., Mullineaux, Donal R. (Eds.), 1981, The 1980 eruptions of Mount St. Helens, 1250. U.S. Geological Survey Professional Paper, Washington, pp. 577–600.
Schneider, D.J., Rose, W.I., Kelley, L., 1995. Tracking of 1992 eruption clouds from crater peak of Mount Spurr volcano, Alaska, using AVHRR. U. S. Geol. Surv. Bull. 2139, 27–36.
Schneider, D.J., Rose, W.I., Coke, L.R., Bluth, G.J.S., 1999. Early evolution of a stratospheric volcanic eruption cloud as observed with TOMS and AVHRR. J. Geophys. Res. 104 (D4), 4037–4050.
Stamnes, K., Swanson, R.A., 1981. A new look at the discrete ordinates method for radiative transfer calculations in anistropically scattering atmospheres. J. Atmos. Sci. 38, 387–399.
Wen, S., Rose, W.I., 1994. Retrieval of sizes and total masses of particles in volcanic clouds using AVHRR bands 4 and 5. J. Geophys. Res. 99 (D3), 5421–5431.

Please cite this article as: Prata, A.J., Bernardo, C., Retrieval of volcanic ash particle size, mass and optical depth from a ground-based thermal infrared camera, J. Volcanol. Geotherm. Res (2009), doi:10.1016/j.jvolgeores.2009.02.007